PHYSICAL REVIEW A VOLUME 39, NUMBER 3 FEBRUARY 1, 1989

Single-mode instability in optical bistability

L. A. Orozco* and H. J. Kimble
Department of Physics, University of Texas, Austin, Texas 78712

A. T. Rosenberger
Department of Physics, Southern Methodist University, Dallas, Texas 75275

L. A. Lugiato
Dipartimento di Fisica del Politecnico, 10129 Torino, Italy

M. L. Asquini and M. Brambilla
Dipartimento di Fisica dell'Università, 20133 Milano, Italy

L. M. Narducci
Department of Physics and Atmospheric Science, Drexel University, Philadelphia, Pennsylvania 19104
(Received 4 April 1988)

This paper gives a detailed description of the plane-wave Gaussian models of optical bistability and of the experimental investigations of the single-mode instability induced on a beam of sodium atoms in a cavity by an external driving field. Our goal is to provide a careful comparison of the theoretical and experimental results. We focus on the shape of the instability domain, the nature and behavior of the spontaneous output oscillations produced by the instability, and their frequency dependence on the control parameters. We carry out this comparison using both the plane-wave and Gaussian models. Our analysis shows that the latter is in good quantitative agreement with the experimental results. We investigate in detail the main assumption of the Gaussian model, namely, that the internal cavity field retains the same radial profile as the input field.

I. INTRODUCTION

The search for a quantitative understanding of the behavior of nonlinear optical systems is an especially challenging and fascinating problem. Aside from the matter of potential applications, perhaps the dominant reason for the sustained level of interest in this area of research has been the variety of phenomena that have continued to emerge form theoretical studies and experimental observations.[1-7] Many different systems have come under careful scrutiny over the years: among them the best known and, arguably, the most fundamental configuration involves a collection of two-level atoms in an optical cavity. This, of course, has formed the starting point of all traditional laser theories and has provided the essential ingredient for the discovery of optical bistability.

The most promising strategy for a quantitative investigation of optical instabilities calls for the identification of the simplest realistic theoretical models and of experimental tests designed to match the essential theoretical constraints. On the basis of this criterion it is reasonable to focus on single-mode rather than multimode instabilities even if the latter ones are likely to display a greater dynamical complexity, and to select homogeneously broadened systems in spite of the fact that inhomogeneously broadened media have also displayed their share of very interesting phenomena.[8]

Roughly speaking, we can classify the existing optical devices into two broad classes: active and passive systems. The paradigm of the first class is the laser, while optical bistability is the best known representative of the latter. Active systems, of course, are characterized by the presence of a population inversion, while passive systems become dynamically interesting only when driven by an external source. The earliest single-mode instabilities were discovered in the laser during the 1960s.[9,10] A key role in understanding the essence of their complex behaviors was played by Haken's proof[11] of the equivalence between the single-mode laser equations and the celebrated Lorenz model.[12] This discovery gave added significance to the basic equations of quantum optics and endowed the laser with a chaotic dynamics of its own.

From a practical point of view, the experimental verification of the single-mode theories is within easier reach in passive systems because the problems created by the high-gain requirement in active media do not arise. In addition, passive systems appear to be better suited to minimize the role of transverse effects on the nonlinear dynamics. One of the limitations of most current theoretical models is their reliance on the plane-wave approximation. This approach is beginning to appear inadequate to describe the low-threshold instabilities in homogeneously broadened lasers because transverse variations of the electric field play an important role in laser dynamics and can change the character of the unstable states in a dramatic way.[13] Passive systems driven by an

external source which is mode matched to the fundamental mode of the cavity can support a simple Gaussian field configuration even in the presence of time-dependent oscillations. Thus, while the plane-wave models need to be modified to account for the nonuniform transverse field profile, higher-order transverse modes can be neglected when dealing with passive systems, while this is less likely so in the presence of active media.

The papers quoted in Refs. 14 and 15 discuss the experimental steady-state observation of absorptive and dispersive optical bistability in a homogeneously broadened two-level system of sodium atoms in a optical cavity, and provide a quantitative comparison of the data with the predictions of the single-mode theory of optical bistability. This model was developed in Ref. 16 within the plane-wave approximation, and was generalized later to include transverse effects, under the assumption that the cavity field retains the same Gaussian radial structure of the input field.[17–20] The quantitative agreement between the observations and the theoretical steady-state predictions of the Gaussian mode theory turns out to be very satisfactory without adjustable parameters.

The single-mode instability for two-level optical bistability was predicted in Ref. 21 within the framework of the plane-wave model, and its existence was confirmed by the analysis of the Gaussian model given in Ref. 22. In fact, this paper indicated also that an experimental observation of this effect was indeed feasible. The eventual demonstration of this single-mode instability[23] came with the help of an improved version of the original experimental system[14] which was adapted to increase the bistability parameter according to the theoretical guidelines. This led to the first experimental observation of a single-mode instability; the physical setting that favors the appearance of this phenomenon represents the passive counterpart of the Lorenz-Haken model.

The objective of this paper is to give a detailed description of the experimental investigations of the single-mode instability in optical bistability and to provide a careful comparison between the experimental results and the theoretical predictions of the single-mode theory. We focus, in particular, on the shape of the instability domain, the nature and behavior of the spontaneous oscillations produced by the instability, and their frequency dependence on the control parameters. We carry out this comparison using both the plane-wave and Gaussian models; our analysis shows that the latter is in good quantitative agreement with the experimental results, while the plane-wave model displays disagreements which are often qualitative in nature. We investigate in detail the main assumption of the Gaussian model, namely, that the internal cavity field retains the same radial profile as the input field, and also establish a bridge between the plane-wave and the Gaussian theory by studying the variations of the output oscillations as a function of the ratio R_0/w_0 between the radius of the atomic sample R_0 and the beam waist w_0. In the limit $R_0/w_0 \to 0$, in particular, the Gaussian model reduces to the plane-wave theory.

In Sec. II we review the derivation of the plane-wave single-mode model from the Maxwell-Bloch equations for a unidirectional ring cavity, and summarize its main predictions relative to the single-mode instability. In Sec. III we derive the coupled time-dependent equations for the different transverse modes of a unidirectional ring cavity with spherical mirrors. In Sec. IV we prove for the first time that the Gaussian single-mode model yields an exact stationary solution in the uniform field limit within appropriate additional restrictions on the frequency spacing between adjacent transverse modes; in addition, we summarize the main predictions of this model and discuss the resulting spontaneous oscillations. Section V is devoted to a detailed description of the experiments and to the comparison between experiments and theory. The conclusions of our analysis are presented in Sec. VI.

II. PLANE-WAVE SINGLE-MODE MODEL OF OPTICAL BISTABILITY

The single-mode, plane-wave theory of optical bistability takes its premises from the usual Maxwell-Bloch equations of laser theory with appropriate boundary conditions, and can be derived from these equations after suitable assumptions and simplifications.[3] For completeness we begin with a brief derivation of the single-mode equations, and continue with a summary of their main predictions. Our aim is to review one of the most popular working models of this phenomenon; another goal, perhaps just as important, is to lay out its main assumptions, in preparation for the more accurate description given in Sec. III.

In its simplest setting (see Fig. 1), the bistable system of interest consists of a unidirectional plane-wave ring resonator of length Λ, and a nonlinear medium with longitudinal dimensions L. The resonator has input and output mirrors with an arbitrary energy reflectivity coefficient R (and transmittivity $T=1-R$) and additional ideal reflectors to close the ring. We model the medium as a collection of homogeneously broadened two-level systems with a transition frequency ω_A, and polarization and population relaxation rates denoted by $\gamma_\perp$ and $\gamma_\parallel$. The resonant cavity is driven by an external monochromatic plane wave with a carrier frequency ω_{in}. The objective of the theory is to describe the behavior of the transmitted intensity as a function of the relevant cavity and atomic parameters.

The equations of motion for this system are the well known Maxwell-Bloch equations

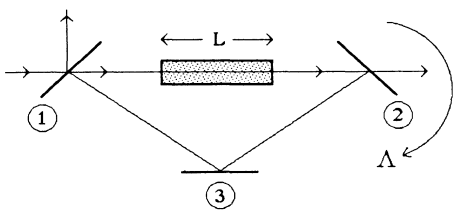

FIG. 1. Schematic representation of the plane-wave ring cavity. The length of the resonator is Λ while that of the nonlinear medium is L. The input and exit mirrors (1 and 2 in the figure) both have energy reflectivity $R=1-T$. Mirror 3 is assumed to be an ideal reflector for simplicity.

$$\frac{\partial F}{\partial z}+\frac{1}{c}\frac{\partial F}{\partial t}=-\alpha P \ , \tag{2.1a}$$

$$\frac{\partial P}{\partial t}=\gamma_{\perp}[FD-(1+i\Delta)P] \ , \tag{2.1b}$$

$$\frac{\partial D}{\partial t}=-\gamma_{\parallel}[\tfrac{1}{2}(FP^{*}+F^{*}P)+D-1] \ , \tag{2.1c}$$

where F is the slowly varying amplitude of the cavity field, normalized to the square root of the saturation intensity, P is the scaled atomic polarization, and D is the scaled population difference between the ground and the excited levels. The parameter Δ, defined by $(\omega_A-\omega_{\rm in})/\gamma_{\perp}$, represents the detuning between the atomic transition frequency and the carrier frequency of the injected field, in units of the atomic linewidth $\gamma_{\perp}$, and α is the field small signal absorption coefficient per unit length.

Equations (2.1) must be supplemented by boundary conditions, which in the case of the ring cavity of Fig. 1 take the form

$$F(0,t)=Ty+RF(L,t-\Delta t)e^{-i\delta_0} \ , \tag{2.2}$$

where y is the scaled amplitude of the incident field, $\Delta t=(\Lambda-L)/c$ is the transit time of light between the exit and the entrance ports of the atomic sample, and δ_0 is the accumulated phase difference per round trip $[\delta_0=(\omega_C-\omega_{\rm in})\Lambda/c]$ due to a possible mismatch between the injected carrier frequency $\omega_{\rm in}$ and the nearest longitudinal cavity resonance ω_C.

While an exact steady-state analysis of Eqs. (2.1) together with the boundary conditions (2.2) can be carried out without excessive complications,[3,24] for the purpose of this paper it is more convenient to focus immediately on an alternative approach based on a modal expansion. The advantage of this procedure is that it provides a clear view of the conditions of validity of the single-mode model.

The introduction of a modal expansion for Eqs. (2.1) is complicated by the presence of finite reflectivity mirrors. A rigorous way to proceed was established in Ref. 25. The essence of this method is to introduce a new set of variables such that the transformed boundary conditions acquire an isochronous, periodic form. This is done in two steps.

(i) First, we define the new set of coordinates

$$z'=z \ , \tag{2.3a}$$

$$t'=t+\frac{\Lambda-L}{c}\frac{z}{L} \ , \tag{2.3b}$$

whose purpose is to make the boundary conditions (2.2) isochronous.

(ii) Next, we introduce the field and atomic variables

$$F_1(z',t')=F(z',t')\exp\left[\frac{z'}{L}(\ln R-i\delta_0)\right]+\frac{Ty}{L}z' \ , \tag{2.4a}$$

$$P_1(z',t')=P(z',t')\exp\left[\frac{z'}{L}(\ln R-i\delta_0)\right] \ , \tag{2.4b}$$

$$D_1(z',t')=D(z',t') \ , \tag{2.4c}$$

whose function is to eliminate from the boundary conditions the multiplicative factors R and $\exp(-i\delta_0)$, an the additive term proportional to the injected field amplitude.

After carrying out the transformations (2.3) and (2.4), the new Maxwell-Bloch equations take the form

$$\frac{\partial F_1}{\partial t'}+\frac{cL}{\Lambda}\frac{\partial F_1}{\partial z'}=\frac{cT}{\Lambda}y+\frac{c}{\Lambda}(\ln R-i\delta_0)\left[F_1-\frac{Ty}{L}z'\right]-\frac{c|\ln R|}{\Lambda}\frac{\alpha L}{|\ln R|}P_1 \ , \tag{2.5a}$$

$$\frac{\partial P_1}{\partial t'}=\gamma_{\perp}\left[D_1\left[F_1-\frac{Ty}{L}z'\right]-(1+i\Delta)P_1\right] \ , \tag{2.5b}$$

$$\frac{\partial D_1}{\partial t'}=-\gamma_{\parallel}\left\{\frac{1}{2}\left[P_1\left[F_1-\frac{Ty}{L}z'\right]\exp\left[-2z'\frac{\ln R}{L}\right]+\text{c.c.}\right]+D_1-1\right\} \ , \tag{2.5c}$$

and the boundary conditions become

$$F_1(0,t')=F_1(L,t') \ . \tag{2.6}$$

The new equations of motion differ from the original ones in several ways.

(i) The phase velocity of the new field amplitude F_1 is cL/Λ instead of c; thus the transformation introduces an effective background index of refraction that accounts for the field retardation due to the empty section of the cavity. (ii) The equations develop an explicit spatial dependence. (iii) The boundary conditions are of the standard periodicity type.

The main virtue of the new picture is that the required solutions are consistent with a modal decomposition of the Fourier type which allows the identification of an exact set of modal amplitudes in the presence of cavity losses. Consider, in fact, the Fourier decomposition

$$\begin{bmatrix}F_1(z',t')\\P_1(z',t')\\D_1(z',t')\end{bmatrix}=\sum_{n=-\infty}^{+\infty}e^{ik_nz'}\begin{bmatrix}f_n(t')\\p_n(t')\\d_n(t')\end{bmatrix} \ , \tag{2.7a}$$

$$\begin{bmatrix}F_1^{*}(z',t')\\P_1^{*}(z',t')\end{bmatrix}=\sum_{n=-\infty}^{+\infty}e^{-ik_nz'}\begin{bmatrix}f_n^{*}(t')\\p_n^{*}(t')\end{bmatrix} \ , \tag{2.7b}$$

where the wave numbers k_n are selected in such a way that

$$k_n=\frac{2\pi}{L}n \quad (n=0,\pm1,\pm2,\dots) \ . \tag{2.8}$$

This ensures that the boundary conditions (2.6) are satisfied automatically. Note that $D_1(z',t')$ is a real variable so that

$$d_n(t')=d^{*}_{-n}(t') \ . \tag{2.9}$$

This symmetry relation, of course, does not apply to the modal amplitudes of the field and atomic polarization variables. The modal functions of the ring cavity in the

new reference system are

$$u_n(z')=\frac{1}{\sqrt{L}}e^{ik_n z'} \tag{2.10a}$$

and satisfy the orthonormality condition

$$(u_n,u_m)\equiv\int_0^L dz' u_n^*(z')u_m(z')=\delta_{n,m}\ . \tag{2.10b}$$

It is now a lengthy but simple matter to derive the coupled equations for the modal amplitudes from Eqs. (2.5), using Eqs. (2.7). The result of this calculation is

$$\begin{aligned}\frac{\partial f_n}{\partial t'}+i\alpha_n f_n=&\frac{cT}{\Lambda}y\delta_{n,0}-\frac{c}{\Lambda}(|\ln R|+i\delta_0)f_n\\&-\frac{c|\ln R|}{\Lambda}\frac{\alpha L}{|\ln R|}p_n\\&+\frac{c}{\Lambda}(|\ln R|+i\delta_0)\frac{Ty}{L}\Gamma_n\ ,\end{aligned} \tag{2.11a}$$

$$\frac{\partial p_n}{\partial t'}=\gamma_\perp\left[\sum_{n'}f_{n'}d_{n-n'}-\frac{Ty}{L}\sum_{n'}\Gamma_{n-n'}d_{n'}-(1+i\Delta)p_n\right]\ , \tag{2.11b}$$

$$\begin{aligned}\frac{\partial d_n}{\partial t'}=-\gamma_\parallel\Bigg[&\tfrac{1}{2}\sum_{n',n''}(f_{n'}p_{n''}^*\Phi_{n'-n''-n}+f_{n'}^*p_{n''}\Phi_{n''-n'-n})\\&-\frac{1}{2}\frac{Ty}{L}\sum_{n'}(p_{n'}^*\Psi_{n+n'}+p_{n'}\Psi_{n-n'})\\&+d_n-\delta_{n,0}\Bigg]\ ,\end{aligned} \tag{2.11c}$$

where

$$\Gamma_n=\frac{1}{L}\int_0^L dz' e^{-ik_n z'}z'=\begin{cases}\dfrac{L}{2}, & n=0\\ \dfrac{i}{k_n}, & n\neq 0\end{cases} \tag{2.12a}$$

$$\begin{aligned}\Phi_n&=\frac{1}{L}\int_0^L dz' e^{ik_n z'}\exp\left[2\frac{z'}{L}|\ln R|\right]\\&=\frac{1-R^2}{R^2(2|\ln R|+ik_nL)}\ ,\end{aligned} \tag{2.12b}$$

$$\begin{aligned}\Psi_n&=\frac{1}{L}\int_0^L dz' z' e^{ik_n z'}\exp\left[2\frac{z'}{L}|\ln R|\right]\\&=-\frac{1-R^2}{R^2}\frac{iL}{2|\ln R|+ik_nL)^2}\ ,\end{aligned} \tag{2.12c}$$

and

$$\alpha_n=\frac{2\pi cn}{\Lambda}\equiv n\alpha_1\quad(n=0,\pm1,\pm2,\ldots)\ . \tag{2.13}$$

The parameters Φ_n and Ψ_n are mode-mode coupling coefficients, while the constant Γ_n couples the incident field to the nth cavity mode [see Eq. (2.11a)]. Note that α_1 is the frequency spacing between adjacent longitudinal resonances, while α_n is the frequency of the nth mode measured from the reference frequency ω_C (i.e., the optical frequency of the nth mode is $\omega_n=\omega_C+\alpha_n$).

The coupled-mode equations (2.11) are exactly equivalent to the original Maxwell-Bloch equations (2.1) or to their transformed version (2.5). Their complexity is obvious by inspection. It is also clear that the evolution of this system is of the multimode type, at least for arbitrary values of the parameters. In order to derive the single-mode equations we assume the validity of the uniform field approximation[3,26]

$$\alpha L\to 0,\quad T\to 0,\quad \delta_0\to 0\ , \tag{2.14a}$$

with

$$2C\equiv\frac{\alpha L}{T},\quad \Theta\equiv\frac{\delta_0}{T}\ , \tag{2.14b}$$

both being arbitrary. With the help of Eqs. (2.14) the modal equations take the form

$$\frac{df_n}{dt'}+i\alpha_n f_n=-\kappa[(1+i\Theta)f_n-y\delta_{n,0}+2Cp_n]\ , \tag{2.15a}$$

$$\frac{dp_n}{dt'}=\gamma_\perp\left[\sum_{n'}f_{n'}d_{n-n'}-(1+i\Delta)p_n\right]\ , \tag{2.15b}$$

$$\frac{dd_n}{dt'}=-\gamma_\parallel\left[\tfrac{1}{2}\sum_{n'}(f_{n'}p_{n'-n}^*+f_{n'}^*p_{n+n'})+d_n-\delta_{n,0}\right]\ , \tag{2.15c}$$

where $\kappa\equiv cT/\Lambda$ represents the cavity linewidth. The equations for f_n^* and p_n^* follow from (2.15a) and (2.15b) upon complex conjugation. Note that in arriving at Eq. (2.15c) we have used the limit

$$\lim_{T\to 0}\Phi_p=\delta_{p,0}\ . \tag{2.16}$$

We are now in the position to prove the following important statement: in the uniform field limit and in steady state, only the amplitudes of the $n=0$ modes are different from zero, i.e., in steady state the cavity field configuration is of the single-mode type. This result emerges from the following considerations. For any $n\neq 0$ and in steady state, the field equation (2.15a) can be written in the form

$$f_n=\frac{iT}{2\pi n}[(1+i\Theta)f_n+2Cp_n]\ . \tag{2.17}$$

Clearly, as T approaches zero, f_n vanishes as well. Next, we consider the steady-state atomic equations for p_n, p_{-n}^*, and d_n for any value $n\neq 0$, and keep in mind that $f_{n\neq 0}=O(T)$. The result if a set of three linear homogeneous equations for which only the trivial solution is possible. Thus, more precisely, we have

$$p_n,p_{-n}^*,d_n=O(T)\quad(n\neq 0)\ . \tag{2.18}$$

It follows that the only nonvanishing amplitudes in steady state are those corresponding to the $n=0$ mode. In order to insure that the time-dependent behavior of the system is also of the single-mode type, a sufficient

condition is provided by the limit

$$\frac{\Lambda\gamma_\perp}{c}\to 0 , \tag{2.19}$$

whose effect is to push every cavity mode, except for the resonant one, so far away from the atomic absorption line that any active role on their part is effectively excluded.

In conclusion, the uniform field condition [Eqs. (2.14)] supplemented by the requirement (2.19) insures that the dynamics of the bistable system is governed by the single-mode equations[16]

$$\frac{dx}{dt'}=-\kappa[(1+i\Theta)x-y+2Cp] , \tag{2.20a}$$

$$\frac{dp}{dt'}=\gamma_\perp[xD-(1+i\Delta)p] , \tag{2.20b}$$

$$\frac{dd}{dt'}=-\gamma_\parallel[\tfrac{1}{2}(xp^*+x^*p)+d-1] , \tag{2.20c}$$

where we have introduced the more familiar notations

$$x\equiv f_0,\quad p\equiv p_0,\quad d\equiv d_0 .$$

The variables x^* and p^* obey the complex conjugate equations of (2.20a) and (2.20b), respectively.

The model embodied by Eqs. (2.20) was formulated from first principles by Bonifacio and Lugiato.[16] In steady state, it leads to the well-known state equation

$$y^2=|x|^2\left[\left[1+\frac{2C}{1+\Delta^2+|x|^2}\right]^2+\left[\Theta-\frac{2C\Delta}{1+\Delta^2+|x|^2}\right]^2\right] . \tag{2.21}$$

When the bistability parameter C is larger than a minimum value $C_{\min}$ that depends on Δ and Θ, the stationary curve for the transmitted intensity $|x|^2$ as a function of the incident intensity y^2 is S shaped, and one obtains bistable behavior. In the resonant case $\Delta=\Theta=0$, the minimum value of C is 4. With appropriate variations of the external control parameters, a segment of the positive-slope part of the stationary curve can become unstable; in this case the transmitted intensity develops oscillatory behavior. This possibility was advanced by Bonifacio and Lugiato[26] and by McCall.[27] Ikeda[28] then showed that under appropriate conditions, the spontaneous oscillations that emerge from this instability can also be chaotic.

A linear stability analysis of Eqs. (2.20) around an arbitrary steady state of the system leads to a fifth-degree polynomial equation for the exponential rate constants that govern the linearized evolution (characteristic equation). The explicit form of this equation is rather cumbersome to derive and is given below for completeness. If λ denotes the complex rate constant in units of $\gamma_\perp$, the characteristic equation is

$$\lambda^5+a_1\lambda^4+a_2\lambda^3+a_3\lambda^2+a_4\lambda+a_5=0 , \tag{2.22}$$

where

$$a_1=2+\gamma+2\kappa' , \tag{2.23a}$$

$$a_2=2\gamma+1+\Delta^2+\gamma|x_{\rm st}|^2+2\kappa'(2+\gamma)+4\kappa' C\frac{1+\Delta^2}{1+\Delta^2+|x_{\rm st}|^2}+\kappa'^2(1+\Theta^2) , \tag{2.23b}$$

$$a_3=\gamma(1+\Delta^2+|x_{\rm st}|^2)+2\kappa'(2\gamma+1+\Delta^2+\gamma|x_{\rm st}|^2)+\kappa'^2(1+\Theta^2)(\gamma+2)+4C\kappa'(\kappa'+\gamma+1)\frac{1+\Delta^2}{1+\Delta^2+|x_{\rm st}|^2}-2C\kappa'\frac{\gamma|x_{\rm st}|^2}{1+\Delta^2+|x_{\rm st}|^2} , \tag{2.23c}$$

$$a_4=2\kappa'\gamma(1+\Delta^2+|x_{\rm st}|^2)+\kappa'^2(1+\Theta^2)(2\gamma+1+\Delta^2+\gamma|x_{\rm st}|^2)+\left[2C\kappa'\frac{1+\Delta^2}{1+\Delta^2+|x_{\rm st}|^2}\right]^2-2C\kappa'^2\gamma|x_{\rm st}|^2\frac{1+\Delta\Theta}{1+\Delta^2+|x_{\rm st}|^2}+4C\kappa'\frac{1+\Delta^2}{1+\Delta^2+|x_{\rm st}|^2}[\gamma(\kappa'+1)+\kappa'(1-\Delta\Theta)], \tag{2.23d}$$

$$a_5=\kappa'^2\gamma(1+\Theta^2)(1+\Delta^2+|x_{\rm st}|^2)+4C\kappa'^2\gamma\frac{1+\Delta^2}{1+\Delta^2+|x_{\rm st}|^2}(1-\Delta\Theta)+\gamma\left[2C\kappa'\frac{1+\Delta^2}{1+\Delta^2+|x_{\rm st}|^2}\right]^2-\gamma|x_{\rm st}|^2(1+\Delta^2)\left[\frac{2C\kappa'}{1+\Delta^2+|x_{\rm st}|^2}\right]^2 . \tag{2.23e}$$

Note that a_5 can also be written in the form

$$a_5=\kappa'^2\gamma(1+\Delta^2+|x_{\rm st}|^2)\frac{d(y^2)}{d(|x_{\rm st}|^2)} . \tag{2.24}$$

In Eqs. (2.23) the symbols κ' and γ denote the cavity linewidth in units of atomic linewidth and the ratio $\gamma_\parallel/\gamma_\perp$, respectively. Because, as noted below, the inequality $a_i<0$, for any $i=1,2,\ldots,5$, implies that the

steady state is unstable, it is clear that the negative-slope part of the steady-state equation is automatically included within the unstable states, in view of Eq. (2.24).

According to the Routh-Hurwitz criterion[29] the complex roots of Eq. (2.22) have negative real parts (i.e., the selected steady state is stable) if and only if

$$a_i > 0 \quad (i=1,2,\ldots,5) \tag{2.25a}$$

and

$$H_i > 0 \quad (i=1,2,\ldots,5) , \tag{2.25b}$$

where H_i are the so-called principal subdeterminants of the Hurwitz quadratic form. For convenience, their explicit form is given in the following:

$$H_1 = a_1 , \tag{2.26a}$$

$$H_2 = a_1 a_2 - a_3 , \tag{2.26b}$$

$$H_3 = a_1(a_2 a_3 - a_1 a_4) - a_3^2 + a_1 a_5 , \tag{2.26c}$$

$$H_4 = a_1[-a_5(a_2^2 - a_4) + a_4(a_2 a_3 - a_1 a_4)] + a_5(a_2 a_3 - a_5) + a_4(a_1 a_5 - a_3^2) , \tag{2.26d}$$

$$H_5 = a_5 H_4 . \tag{2.26e}$$

A useful tool for comparing the theoretical predictions with the experimental results is the boundary of the instability domain in an appropriate plane of control parameters. The instability boundary predicted by the plane-wave theory, however, is in poor agreement with the experimental results, as we show in Sec. V, so that further discussion of the results of the linear-stability analysis will not be necessary.

Within the unstable domain, the plane-wave theory of optical bistability predicts a variety of single-mode-pulsation phenomena, in addition to interesting dynamical effects of the multimode type. Here we focus only on the unstable behaviors that are connected with the single-mode model.[21,22] When the incident field, the atoms, and the cavity are exactly in resonance ($\Delta=\Theta=0$) no positive-slope instability exists. For increasing values of the mismatch between the carrier frequency of the incident field and the cavity frequency, the system may no longer be able to follow the driving action of the external signal and the stationary state becomes destabilized.

This instability can develop either in the presence or in the absence of bistability (i.e., with an S-shaped or with a single-valued stationary curve). A characteristic signature of this instability is that it arises most easily (but not exclusively) when the atomic and cavity detunings have opposite signs, i.e., with $\Delta\Theta < 0$. When the bistability parameter is of the order of 50, the spontaneous oscillations are periodic and display a frequency of the order of the cavity detuning, $\omega_C - \omega_{in} = \Theta\kappa$. For larger values of C (C greater than about 300) the oscillations display period doubling and even chaos (Fig. 2). In fact, the emergence of these behaviors is rather common within the context of the plane-wave theory. The picture that emerges from the experiments, on the other hand, shows that several aspects of this theoretical development are entirely inadequate. For this reason, a more accurate handling of the cavity field is necessary, as discussed in Sec. III.

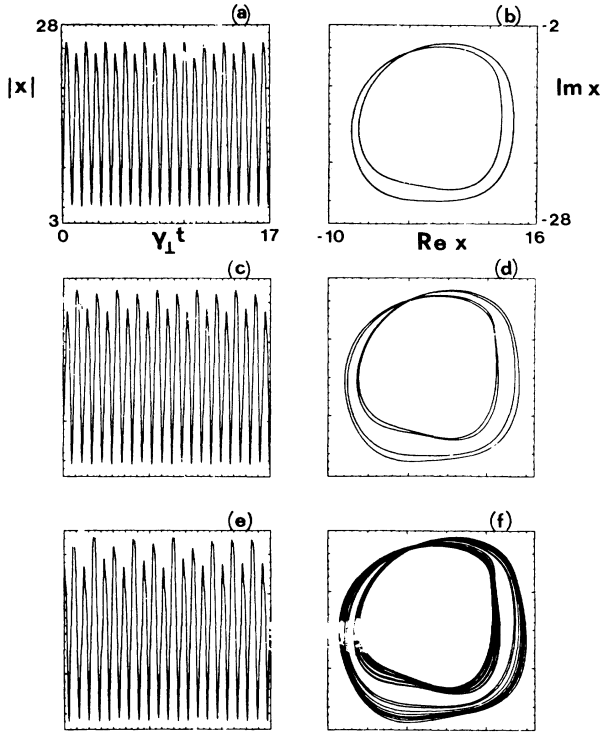

FIG. 2. Self-oscillations from the numerical solution of Eqs. (2.20) for $C=400$, $\Delta=-1$, $\Theta=20$, $\kappa'=0.4$, and $\gamma=1.76$. (a), (c), and (e) show the normalized transmitted field $|x|$ as a function of $\gamma_\perp t$; (b), (d), and (f) show the projection of the phase-space trajectory in the plane (Rex, Imx); (a) period 2 for $y=309.1$; (b) period 4 for $y=303$; (c) chaos for $y=297.3$.

III. RADIALLY VARYING ELECTRIC FIELD

In this section we consider the more realistic situation in which the dynamical variables F, P, and D are allowed to vary along the radial direction. For this purpose we consider the ring-cavity configuration sketched in Fig. 3. In the paraxial approximation, the Maxwell-Bloch equations take the form[20]

$$\frac{1}{2ik_{in}}\nabla_\perp^2 F + \frac{\partial F}{\partial z} + \frac{1}{c}\frac{\partial F}{\partial t} = -\alpha P , \tag{3.1a}$$

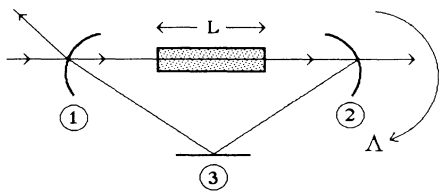

FIG. 3. Schematic representation of the ring cavity with spherical mirrors.

$$\frac{\partial P}{\partial t}=\gamma_{\perp}[FD-(1+i\Delta)P] , \tag{3.1b}$$

$$\frac{\partial D}{\partial t}=-\gamma_{\parallel}[\tfrac{1}{2}(FP^*+F^*P)+D-\chi(r,z)] , \tag{3.1c}$$

where F is the normalized slowly varying amplitude of the electric field, P is the scaled atomic polarization, and D the scaled population difference between the ground and excited levels. The wave number k_{in} is defined as ω_{in}/c where ω_{in} is the carrier frequency of the injected field, and the parameters α, $\gamma_{\perp}$, $\gamma_{\parallel}$, and Δ have the same meaning as described in Sec. II.

Under the assumption of cylindrical symmetry around the longitudinal z axis, the transverse Laplacian $\nabla_{\perp}^2$ takes the form

$$\nabla_{\perp}^2\equiv\frac{\partial^2}{\partial r^2}+\frac{1}{r}\frac{\partial}{\partial r} ,$$

where r is the radial variable. The term $\nabla_{\perp}^2F$ in the field equation (3.1a) describes the diffraction of the cavity field; $\chi(r,z)$ plays the role of a characteristic function for the atomic sample and is defined by

$$\chi(r,z)=\begin{cases}1 \quad \text{for } |z|<\dfrac{L}{2}, \quad r<R_0\\ 0 \quad \text{otherwise,}\end{cases} \tag{3.2}$$

where L and R_0 denote the length and the radius of the atomic sample, respectively. The structure of the transverse modes for a cavity of the type shown in Fig. 3 has been known for a long time[30] and has been reviewed in some detail in Ref. 31. These are given by

$$A_p(r,z)=\frac{\sqrt{2/\pi}}{w(z)}\exp\left[-\frac{r^2}{w^2(z)}\right]L_p\left[\frac{2r^2}{w^2(z)}\right]\times\exp[i\phi_p(r,z)] , \tag{3.3}$$

where $L_p(x)$ is the Laguerre polynomial of order p and the indicated argument, and where

$$w(z)=w_0[1+(z/z_0)^2]^{1/2} , \tag{3.4}$$

$$\phi_p(r,z)=k_{\text{in}}\frac{r^2}{2R(z)}-(2p+1)\tan^{-1}(z/z_0) , \tag{3.5}$$

$$R(z)=\frac{1}{z}(z^2+z_0^2) . \tag{3.6}$$

The symbol w_0 represents the beam waist and z_0 is the Rayleigh length

$$z_0=\frac{\pi w_0^2}{\lambda} , \tag{3.7}$$

with $\lambda=2\pi/k_{\text{in}}$. The functions $A_p(r,z)$ are solutions of the free-field equation

$$\nabla_{\perp}^2A_p+2ik_{\text{in}}\frac{\partial A_p}{\partial z}=0 \tag{3.8}$$

and obey the orthonormality relation

$$2\pi\int_0^{\infty}dr\,rA_p^*(r,z)A_{p'}(r,z)=\delta_{p,p'} . \tag{3.9}$$

The explicit expression of the beam waist w_0 as a function of the cavity parameters is given in Ref. 31 and can be adapted easily to different cavity geometries. After inserting the expansion

$$E(r,z,t)=\sum_{p=0}^{\infty}f_p(z,t)A_p(r,z) \tag{3.10}$$

into Eq. (3.1a) and taking Eq. (3.9) into account, we obtain the following set of equations for the modal amplitudes f_p:

$$\frac{\partial f_p}{\partial z}+\frac{1}{c}\frac{\partial f_p}{\partial t}=-\alpha\int_0^{\infty}dr\,2\pi rA_p^*(r,z)P(r,z,t) . \tag{3.11}$$

In the case of a resonator with spherical mirrors and cylindrical symmetry the cavity frequencies $\omega_{n,p}$ are labeled by two indices. The index $p=0,1,2,\ldots$ refers to the transverse structure, while the longitudinal index $n=0,\pm1,\pm2,\ldots$ has the same meaning as in Sec. II (for example, $\omega_{0,0}=\omega_C$). If we assume that the incident field is matched to the mode $p=0$, the boundary conditions for the amplitudes f_P are[20]

$$f_p(-L/2,t)=Ty_0\delta_{p,0}+Re^{-i\delta_p}f_p\left[L/2,t-\frac{\Lambda-L}{c}\right], \tag{3.12}$$

where y_0 is the normalized amplitude of the incident field, T and $R\equiv1-T$ are the energy transmittivity and reflectivity coefficients of the spherical mirrors, respectively, Λ is the total cavity length, and δ_p is defined by

$$\delta_p=\frac{\omega_p-\omega_{\text{in}}}{c/\Lambda} , \tag{3.13}$$

where $\omega_p\equiv\omega_{0,p}$ is the resonance frequency of the $(0,p)$ mode whose explicit expression can be found in Ref. 31.

When the Rayleigh length z_0 is much larger than the length L of the sample, the beam radius is practically constant through the medium, i.e., $w(z)\approx w_0$. Furthermore, if p is not too large, we can replace the phase factor $\exp[i\phi_p(r,z)]$ with unity in Eq. (3.3), so that the expression for $A_p(r,z)$ takes the approximate form

$$A_p(r)=\frac{\sqrt{2/\pi}}{w_0}\exp[-(r/w_0)^2]L_p[2(r/w_0)^2] . \tag{3.14}$$

In steady state, with all the time derivatives equal to zero, and after inserting the expansion (3.10) into Eqs. (3.1b) and (3.1c), we obtain the stationary equation for the modal amplitudes

$$\frac{df_p}{dz}=-\alpha\int_0^{\infty}dr\,2\pi r\chi(r,z)A_p^*(r,z)\times\frac{(1-i\Delta)\sum_{p'}A_{p'}(r,z)f_{p'}(z)}{1+\Delta^2+\left|\sum_{p'}A_{p'}(r,z)f_{p'}(z)\right|^2} , \tag{3.15}$$

whose boundary conditions are

$$f_p(-L/2)=Ty_0\delta_{p,0}+Re^{-i\delta_p}f_p(L/2) . \tag{3.16}$$

IV. ANALYSIS OF THE GAUSSIAN MODEL

A useful approximate model which has been analyzed extensively to study the possible steady states of the bistable system and their linear stability properties[17,20–22] follows by neglecting all the field amplitudes f_p for $p \neq 0$. Upon setting

$$x(t)=\left[\frac{2}{\pi}\right]^{1/2}\frac{1}{w_0}f_0(t), \quad y=\left[\frac{2}{\pi}\right]^{1/2}\frac{1}{w_0}y_0 , \tag{4.1}$$

the equations describing this model are

$$\kappa^{-1}\frac{dx(t)}{dt}=-\left[(1+i\Theta)x-y+2C\int_0^{R_0/w_0}d\rho\, 4\rho e^{-\rho^2}P(\rho,t)\right] , \tag{4.2a}$$

$$\gamma_\perp^{-1}\frac{\partial}{\partial t}P(\rho,t)=D(\rho,t)x(t)e^{-\rho^2}-(1+i\Delta)P(\rho,t) , \tag{4.2b}$$

$$\gamma_\parallel^{-1}\frac{\partial}{\partial t}D(\rho,t)=-\tfrac{1}{2}[P(\rho,t)x^*(t)+P^*(\rho,t)x(t)]e^{-\rho^2}-D(\rho,t)+\chi , \tag{4.2c}$$

where $\rho=r/w_0$. The model described by Eqs. (4.2) is based on the assumption that the Rayleigh length z_0 is much larger than the sample length; in this case, the lowest order mode A_0 is given by Eq. (3.14) with $p=0$. Furthermore, the longitudinal uniformity of the variables x, P, and D requires the uniform field limit (2.14).

It is common to justify the validity of the single-transverse-mode approximation on the basis of the diffractive mixing which is characteristic of a cavity whose Fresnel number $w_0^2/\lambda\Lambda$ is of order unity, or with the assumption that the higher-order transverse modes ($p>0$) have sufficiently high losses. Apparently, however, no exact argument has ever been proposed to justify this approximation in more rigorous terms. We now show that Eq. (4.2), or their obvious generalization when z_0 is not much larger than L, yield *the exact stationary solution of the spherical resonator problem in the uniform field limit* (2.14) and under the additional requirement that the transverse modes are non degenerate. The latter statement is equivalent to the conditions

$$\delta_0=O(T),\delta_p-2\pi n=O(T^0) , \tag{4.3}$$

for $p=1,2,\ldots$ and any integer n. It is clear from Eq. (3.15) that, for $\alpha L \ll 1$, the variation of the modal amplitude f_p along the atomic sample is negligible. In fact, to first order in αL, we have

$$f_p(L/2)-f_p(-L/2)=-\alpha\int_{-L/2}^{L/2}dz\int_0^\infty dr\, 2\pi r\chi(r,z)A_p^*(r,z)\frac{(1-i\Delta)\sum_{p'}A_{p'}(r,z)f_{p'}(L/2)}{1+\Delta^2+\left|\sum_{p'}A_{p'}(r,z)f_{p'}(L/2)\right|^2} . \tag{4.4}$$

On the other hand, from Eq. (3.16) we find

$$f_p(L/2)-f_p(-L/2)=f_p(L/2)(1-Re^{-i\delta_p})-Ty_0\delta_{p,0} . \tag{4.5}$$

If we now take into account that $\delta_0=O(T)$, and neglect terms of order T^2, the boundary condition for the $p=0$ field amplitude becomes

$$f_0(L/2)-f_0(-L/2)=f_0(L/2)(T+i\delta_0)-Ty_0 . \tag{4.6}$$

In terms of the definitions of C and Θ [Eq. (2.14b)] and with the help of Eq. (3.2), the stationary field equation can be written in the form

$$y_0=f_0(L/2)(1+i\Theta)+2C\frac{1}{L}\int_{-L/2}^{+L/2}dz\int_0^{R_0}dr\, 2\pi r A_0^*(r,z)\frac{(1-i\Delta)\sum_{p'}A_{p'}(r,z)f_{p'}(L/2)}{1+\Delta^2+\left|\sum_{p'}A_{p'}(r,z)f_{p'}(L/2)\right|^2} . \tag{4.7}$$

For $p>0$, instead, Eqs. (4.4) and (4.5) lead to

$$f_p(L/2)=-\frac{\alpha L}{1-R\exp(-i\delta_p)}\frac{1}{L}\int_{-L/2}^{+L/2}dz\int_0^\infty dr\, 2\pi r A_p^*(r,z)\frac{(1-i\Delta)\sum_{p'}A_{p'}(r,z)f_{p'}(L/2)}{1+\Delta^2+\left|\sum_{p'}A_{p'}(r,z)f_{p'}(L/2)\right|^2} . \tag{4.8}$$

Because $\delta_P-2\pi n=O(T^0)$ for $p>0$ and any integer n, it follows that $f_p(L/2)$ is of the order of αL and, therefore, it vanishes in the limit (2.14). This proves that only the fundamental mode survives in this limit; as a result the equation of state becomes

$$y_0=f_0(L/2)\left[1+i\Theta+2C\frac{1}{L}\int_{-L/2}^{+L/2}dz\int_0^{R_0}dr\, 2\pi r\frac{(1-i\Delta)|A_0(r,z)|^2}{1+\Delta^2+|A_0(r,z)f_0(L/2)|^2}\right] . \tag{4.9}$$

If z_0 is much greater than L, with the help of Eqs. (3.14) and (4.1), we can write Eq. (4.9) in the simpler form

$$y=x\left\{1+i\Theta+2C\int_0^{R_0/w_0}d\rho\,4\rho\frac{(1-i\Delta)\exp(-2\rho^2)}{1+\Delta^2+|x|^2\exp(-2\rho^2)}\right\}, \tag{4.10}$$

which coincides with the steady-state equation of the model (4.2).[20] It is also clear that, if the incident field is not matched to the fundamental cavity mode but to a higher-order one (say, $p'\neq 0$) the behavior of the system will again be of the single-mode type; this time, however, the steady-state field will correspond to the cavity mode $p=p'$. This conclusion requires the validity of the limits $\alpha L\to 0$, $T\to 0$, and $\delta_{p'}\to 0$, with $C=\alpha L/2T$ and $\Theta_{p'}=\delta_{p'}/T$ constant and arbitrary and with $\delta_p=O(T^0)$ for $p\neq p'$.

In the experiments on optical bistability with sodium atomic beams,[14,15] αL can be larger than unity and the confocal cavity has a high degree of modal degeneracy. In spite of these facts, as described in detail in Ref. 14 and 15, the steady-state equation (4.12) fits the steady-state experimental data quite well as already shown in Ref. 14(b).

Up to this point we have focused only on the steady-state behavior. In order to ensure that also the time-dependent evolution remains of the single-mode type a sufficient condition is provided by the limit (2.19) whose effect is to move all longitudinal and transverse modes, except for the resonant one, very far away from the atomic line. As a result these modes remain always unexcited.

The linear-stability analysis of the stationary solutions of the model (4.2) was described in detail in Ref. 22. The boundary of the instability domain in the space of the system parameters and the oscillation frequency ν on this boundary are given by the equations

$$G_+(\nu',\Pi)=1,\quad \nu'=\kappa' D_+(\nu',\Pi)\,, \tag{4.11a}$$

or

$$G_-(\nu',\Pi)=1,\quad \nu'=\kappa' D_-(\nu',\Pi)\,, \tag{4.11b}$$

where $\nu'=\nu/\gamma_\perp$ and Π denotes the set of independent parameters C, Δ, Θ, κ', γ, and x. The explicit expressions of the functions $G_\pm(\nu',\Pi)$ and $D_\pm(\nu',\Pi)$ are given in Ref. 22. The instability boundary is obtained by eliminating ν' between the first and second of Eqs. (4.11a) or (4.11b) and the oscillation frequency on the boundary follows immediately from the second of Eqs. (4.11a) or (4.11b).

The discussion in Ref. 22 deals mainly with the situation in which $\gamma_\parallel\approx 2\gamma_\perp$, and $\kappa\approx 0.5\gamma_\perp$. It turns out that for $\Delta\Theta<0$, with Δ of the order of unity and Θ of several units, the stationary state displays extended unstable regions if C is larger than about 50. These unstable regions appear both in the presence or in the absence of bistability. In the former case the steady-state curve is S shaped and the instability develops in the positive-slope part of the upper branch (the instability of the negative-slope branch of the state equation is of a more trivial type and does not lead to self-oscillations). A simultaneous change in sign in Δ and Θ does not alter the details of the behavior of the system.

We have investigated the spontaneous oscillations produced by this instability with a numerical integration of Eqs. (4.2), using $\gamma_\parallel\approx 2\gamma_\perp$, $\kappa\approx 0.5\gamma_\perp$, and $R_0/w_0\gg 1$, in line with the experimental conditions. Figure 4 shows the oscillations when the input intensity is scanned slowly for $C=55$, $\Delta=2.5$, $\Theta=-25$, $\kappa'=0.32$, and $\gamma=1.6$; Figs. 4(a) and 4(b) correspond to the forward scan, while Figs. 4(c) and 4(d) to a backward scan. Figures 4(b) and 4(d) are produced after filtering the oscillations so that the average becomes apparent. Figure 5 is similar to 4 but it corresponds to a much larger value of the bistability parameter ($C=300$). The steady-state curve is single valued; we recognize, however, a range of the input intensity, $2.5\times 10^5<y^2<3.5\times 10^5$, where stable stationary states coexist with stable oscillatory solutions. For $C<400$ the system produces only simple oscillations with period 1, as shown for example in Fig. 6. The only counterexample corresponds to the bistable domain $2.5\times 10^5<y^2<3.5\times 10^5$ of Fig. 5; here we found breathing behavior in which the envelope itself of the oscillations undergoes oscillatory motion (see Fig. 7). We cannot claim to have undertaken an exhaustive scan of the interesting parameter space; still, our search is suggestive that all higher-order dynamical features (period 2, period 4, . . . , chaos, etc.) displayed by the plane-wave model disappear as one introduces transverse effects. Perhaps this is the consequence of the very different structure of the plane-wave and the Gaussian models, as the radial variations of the latter introduce a new continuum of de-

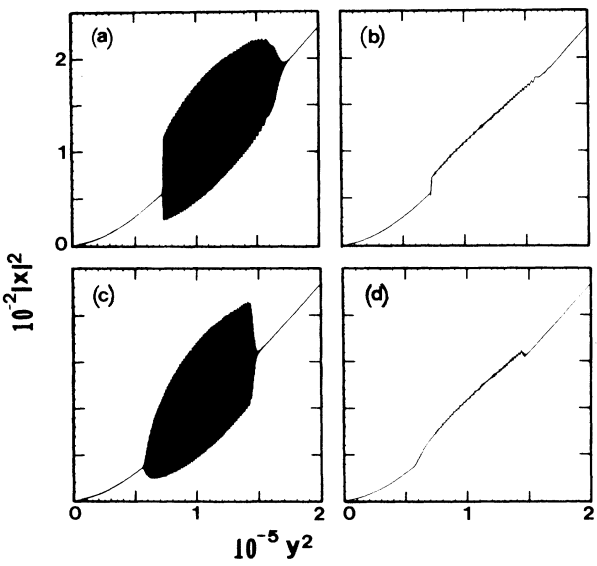

FIG. 4. Spontaneous oscillations in the transmitted intensity as the input intensity is swept slowly for $C=55$, $\Delta=2.5$, $\Theta=-25$, $\kappa'=0.32$, and $\gamma=1.6$; (a) and (b) correspond to a forward scan, (c) and (d) to a backward scan. (b) and (d) show the average behavior of the oscillations.

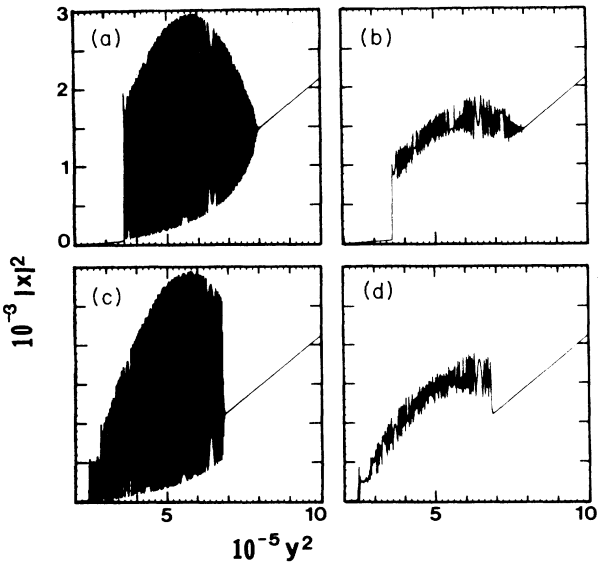

FIG. 5. Same as Fig. 4 with $C=300$, $\Delta=-3$, $\Theta=17$, $\kappa'=0.5$, and $\gamma=1.6$.

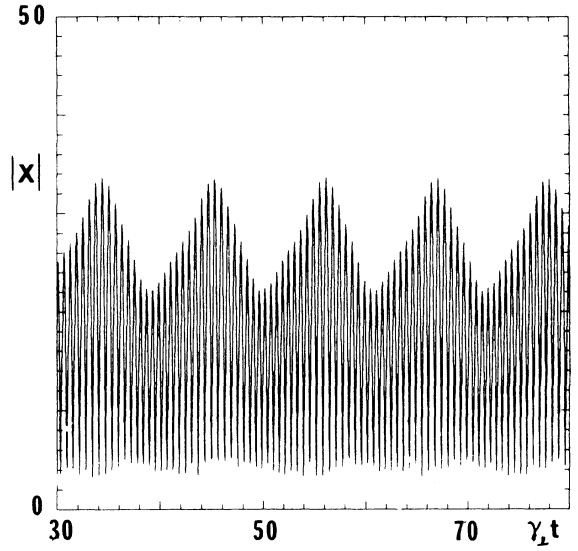

FIG. 7. Envelope breathing of the transmitted intensity for $y=530$. The other parameters are the same as in Fig. 5.

grees of freedom (the values of the dynamical variables at different radial positions).

It is interesting to observe that, in contrast with the simple character of the field oscillations, the atomic polarization and population difference acquire a very complicated radial dependence under unstable conditions. This is illustrated by Fig. 8 which shows the evolution of the functions $\mathrm{Re}[P(\rho,t)]$, $\mathrm{Im}[P(\rho,t)]$, and $D(\rho,t)$ during a few oscillation periods. The stationary configuration of the same functions, shown in Fig. 9 for the same values of the parameters, is given instead by the simple formulas

$$P(\rho)=\frac{1-i\Delta}{1+\Delta^2+|x|^2\exp(-2\rho^2)}x\exp(-\rho^2)\ , \quad (4.12a)$$

$$D(\rho)=\frac{1+\Delta^2}{1+\Delta^2+|x|^2\exp(-2\rho^2)}\ . \quad (4.12b)$$

Thus the assumption that the field maintains a time-

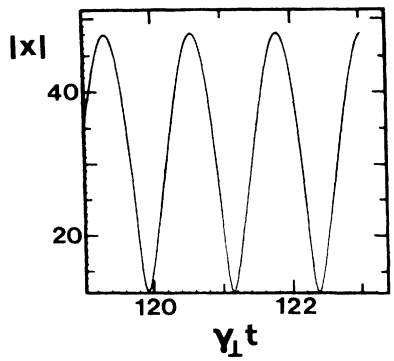

FIG. 6. Self-oscillations predicted by the model (4.2) for $C=300$, $\Delta=3$, $\Theta=-25$, $\kappa'=0.4$, $\gamma=1.6$, and $y=900$. The modulus $|x|$ of the electric field is plotted as a function of $\gamma_\perp t$.

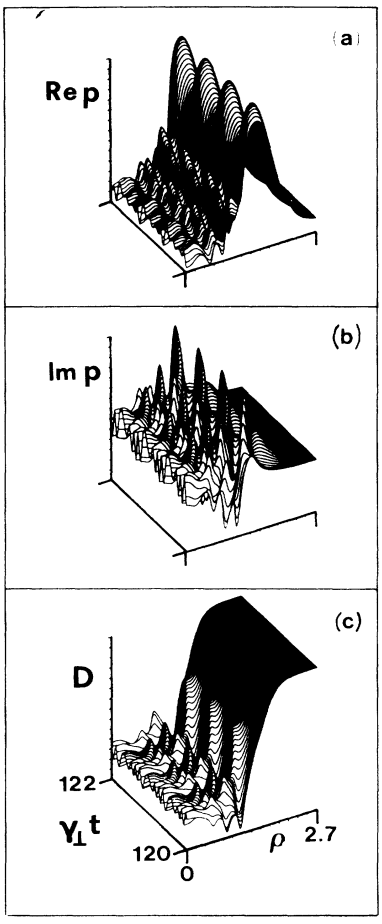

FIG. 8. This figure displays the time evolution of the functions (a) $\mathrm{Re}P(\rho,t)$, (b) $\mathrm{Im}P(\rho,t)$, and (c) $D(\rho,t)$ during the periodic oscillations observed for $C=300$, $\Delta=3$, $\Theta=-25$, $\kappa'=0.5$, $\gamma=1.6$, and $y=900$.

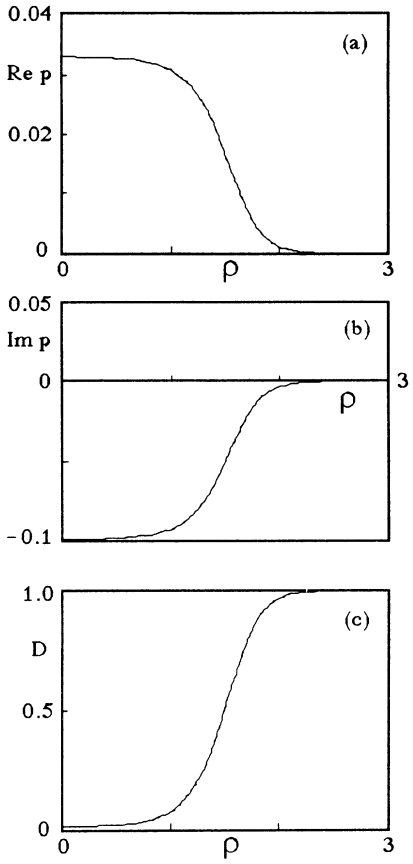

FIG. 9. Radial configuration of (a) $\mathrm{Re}P(\rho)$, (b) $\mathrm{Im}P(\rho)$, and (c) $D(\rho)$ in the stationary state described by Eqs. (4.12). The values of the parameters are the same as in Fig. 7.

independent Gaussian transverse structure in the self-pulsing region implies a complicated radial variation of the atomic variables.

V. EXPERIMENTAL INVESTIGATION OF THE SINGLE-MODE INSTABILITY IN OPTICAL BISTABILITY

A. Experimental apparatus

Our experimental system is designed to fulfil to a great degree the conditions widely employed in theoretical models, two-level atoms interacting with a single mode of the electromagnetic field. The apparatus (Fig. 10) consists of a set of ten well-collimated atomic beams of sodium with ± 1 mrad divergence, 0.5 mm width along the cavity axis, 2 mm depth transverse to the cavity axis, and 1.5 mm center-to-center spacing. The atoms are prepared[32] in the $3\,^2S_{1/2}$, $F=2$, $m_F=2$ state with two lasers, one to transfer the population from the $F=1$ to the $F=2$ hyperfine level of the ground state of the D_2 line of sodium, and the other to align the atoms in the $F=2$, $m_F=2$ sublevel, and thus create an effective two-state system with the highest density possible (Fig. 11). The excitation in the interaction region is produced with circularly polarized light to the $3\,^2P_{3/2}$, $F=3$, $m_F=3$ state. The measured absorption width of 13 MHz is greater than the 10 MHz natural linewidth primarily because of transit broadening; an atom with the most probable speed crosses the waist of the Gaussian beam, $2w_0$,

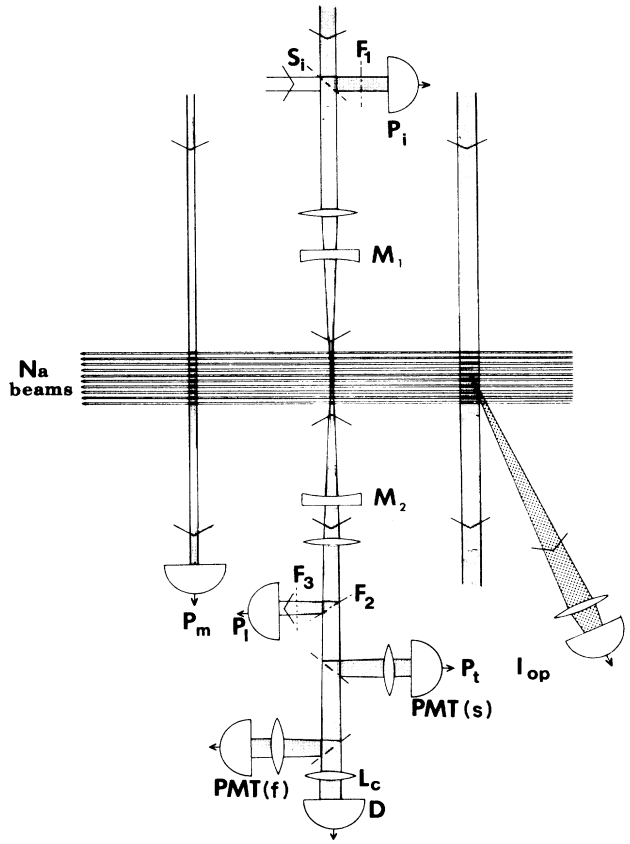

FIG. 10. Experimental setup. Top view: Three laser beams (fine shade) intersect at 90° ten well-collimated atomic beams of sodium. The first beam optically prepumps the atoms but consists of two independent lasers offset by 1.71 GHz to obtain maximum atomic density, with the fluorescence (grainy shade) from one of the center beams (I_{OP}) collected onto a photomultiplier tube. The second laser (signal beam) is mode matched to the cavity formed by mirrors M_1 and M_2. The input power (P_i) is measured by splitting a constant fraction onto a photodiode. A second laser, Zeeman-stabilized He-Ne (not shaded), is mixed with the signal beam at the beam splitter S_i; an interference filter (F_1) is placed in front of the input diode (P_i) to pass only 589-nm light. The output power transmitted through the cavity is first incident on a filter (F_2) which passes only 589-nm light and reflects predominantly the 633-nm beam onto a photodiode (P_1) through the filter F_3 for the 633 nm to lock the cavity. Then the 589-nm light is split onto two photomultiplier tubes: PMT(S), which is externally limited in bandwidth (7 MHz) and serves to record the output characteristics of the system P_t while PMT(f) is a fast photomultiplier whose output is displayed on a spectrum analyzer to identify instabilities. The last part of the output beam is focused with a cylindrical lens L_c onto an array of diodes D to measure the spatial transverse profile of the output field. Further downstream the small-signal absorption is measured with the monitor beam (P_m). The transverse dimensions of the laser beams relative to the atomic beams are exaggerated in the figure.

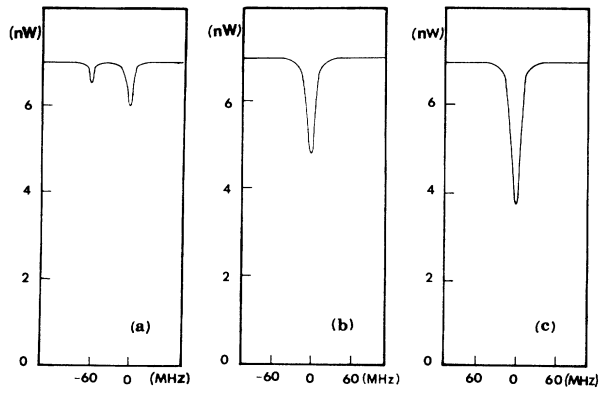

FIG. 11. Transmitted power through the atomic beams as a function of the laser frequency around the $3\,^2S_{1/2}$, $F=2$ to $3\,^2P_{3/2}$, $F=3$ transition in the D_2 line of sodium. The power level is 7 nW. (a) No optical pumping, $\alpha_m L=0.16$. (b) As in (a) but with optical prepumping to restrict the transition to occur only between $F=2$, $m_F=2$ and $F=3$, $m_F=3$; $\alpha_m L=0.38$. (c) As in (b) but with optical pumping by two lasers, the second of which transfers all the population of the $F=1$ ground state to the $F=2$ level; $\alpha_m L=0.63$. Traces *b* and *c* are taken with the same vapor pressure in the oven which produces the atomic beams while trace *a* is for a slightly lower value.

in approximately 12 radiative lifetimes. The beams intersect the TEM_{00} mode of a high-finesse interferometer perpendicularly to within 1 mrad, near midcavity, in a region of homogeneous magnetic field parallel to the cavity axis.

Before the experiments, an absolute measurement of the small-signal absorption $\alpha_m L$ is performed by replacing the output mirror M_2 (Fig. 10) with an antireflection-coated blank. Note that α_m is the measured intensity absorption coefficient, whereas the α defined in Sec. II is the field absorption coefficient. The atomic density is varied by changing the temperature of the oven which produces the atomic beams; a probe power of 7 nW is used; otherwise the geometry is exactly the same as employed in the experiment. The absorption $\alpha_m L$ is related to the optical-pumping fluorescence of one of the center beams (I_{OP}) and to another small-signal absorption (monitor beam P_m) measured downstream from the cavity. These two independent measurements provide knowledge of $\alpha_m L$ during the experiments and give us a check of consistency.

Ring and standing-wave resonators are used (Fig. 12, Table I), all of them derived from a basic resonator that consists of a pair of 1.25-cm-diameter mirrors with 5-cm radius of curvature and the same transmission coefficient $T=(3.0\pm0.1)\times10^{-3}$. Coarse (mechanical) variation in the mirror separation permits us to obtain different cavities, while fine variation is controlled by a voltage applied to the piezoelectric crystal attached to the front mirror M_1. Three standing-wave resonators are used (Fig. 11(b), Table I): one, (a), is at the confocal spacing (5 cm): the others, (b) and (e) are out of confocal and separated by 5.5 cm. The confocal resonator is mode degenerate while the out-of-confocal cavities have a transverse mode spacing of 150 MHz. Two confocal ring configurations, (c) and (d), are also employed by translating the interferometer down 0.5 mm with respect to the incident laser (Fig. 12(a), Table I). This ring-cavity configuration (note that two intracavity beams intersect at a small angle in the atomic beam) allows us to cross the atomic beams four times to achieve higher linear absorption $\alpha_m L$ for a given vapor pressure in the oven. The cavity properties are summarized in Table I.

The incident laser is mode matched to the cavities so that the fundamental TEM_{00} mode is excited with an efficiency greater than 94% (in power). The cavities have a mode waist w_0 of approximately 69 μm. Of the geometries used, (a), (c), and (d) are mode degenerate, while (b) and (e) are not.

A frequency- and intensity-stabilized commerical dye laser with an approximate rms linewidth of 500 kHz is used as the excitation source for the cavity. The power (P_i) entering the cavity (Fig. 12) is measured by splitting a constant fraction onto a photodiode which is calibrated relative to the power incident upon the cavity. The output power transmitted through the cavity is first split onto two photomultiplier tubes PMT(S) and PMT(f) (Fig. 10). PMT(S), which continuously monitors the output characteristics of the system, has its bandwidth limited to about 7 MHz and is calibrated relative to the absolute average power P_t exiting the cavity. PMT(f) is not externally limited in its response time and is used to identify and characterize the instabilities with the aid of a rf spectrum analyzer. PMT(S) provides a way to record the input-output response of the system on resonance in order to cross check the calibrations and provide knowledge of the detunings. The rest of the beam is directed to a third detector *D*, a vertical diode array (reticon), to monitor the shape of the transmitted beam. When the ring cavities are employed, two output beams exit the cavity as shown in Fig. 12(a); in those cases only the upper beam is measured by the output detectors.

Since the instabilities are present only when both cavity and atoms are driven out of resonance, measurements

TABLE I. Summary of cavity properties and decay parameters for the experiments.

Type	F	T_0	κ'	γ'
(a) Confocal standing wave	600±30	0.32±0.01	0.4	1.6
(b) Out-of-confocal standing wave	670±30	0.30±0.01	0.32	1.6
(c) Confocal ring	230±15	0.078±0.006	0.50	1.6
(d) Confocal ring	300±15	0.088±0.007	0.40	1.6
(e) Out-of-confocal standing wave	666±30	0.25±0.01	0.32	1.6

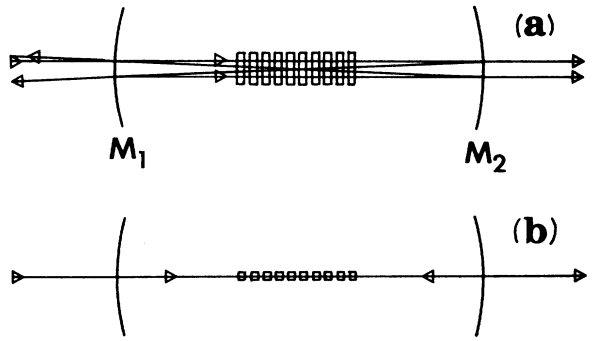

FIG. 12. Cavity configurations for the experiments. Side view facing the atomic beams. (a) Ring configuration with four passes through the atomic medium and (b) standing-wave configuration. The top view of both cavities is the same as shown in Fig. 10.

of the cavity detunings and atomic detunings are necessary. The laser is tuned away from the atomic resonance, and the optical-pumping fluorescence, the line profile of which has been previously calibrated, is measured to determine the detuning. An independent continuously scanned interferometer provides additional information on the laser detuning with respect to the atomic line center. Care is taken not to detune very far from the atomic resonance, because this could reduce the efficiency of the optical pumping.

Tuning of the cavity resonance is achieved by varying the voltage applied to the piezoelectric crystal that controls the fine position of the input mirror M_1. The voltage can be varied manually, thus changing the cavity detuning, or the cavity detuning can be controlled by locking to the transmission fringe of a frequency-tunable Zeeman-stabilized He-Ne laser. For a fixed cavity length, a change in the frequency of the signal laser changes the cavity detuning simultaneously with the atomic detuning.

The cavity detuning is measured by comparing the slope of the input-output response, high in the upper branch of the input-output curve where the atoms are saturated and instabilities are absent, with the resonant empty cavity slope. This is a direct measurement of the detuning provided one is in a region of sufficiently high output intensity, and it does not depend on detector calibrations. As a cross check for the cavity detuning we monitor the voltage applied to the piezoelectric transducer on which the mirror M_1 is mounted, obtaining good agreement with the values inferred from the slope method. The voltage also provides knowledge of the sign of the detuning. As a final check, whenever the cavity is locked to the fringe of the He-Ne laser, we can shift the frequency of the Zeeman-stabilized laser by a known amount and thus measure the cavity detuning. Two locking configurations are used. The first locks to the side of the red transmission fringe. In the second, double passing the red light through an acousto-optic modulator (AOM) and impressing a frequency modulation enables a lock to the peak of the red transmission fringe using standard lock-in techniques.

B. Experimental procedures

The laser beams are first aligned with the atomic beams to ensure perpendicularity and to minimize any Doppler broadening by employing a retroreflected beam from a corner cube prism; next, we calibrate the weak-signal absorption $\alpha_m L$ ($\alpha_m = 2\alpha$) and relate it to the optical-pumping fluorescence $I_{\rm OP}$ and to the weak-signal absorption of P_m, downstream from the interaction region. After this alignment and calibration, the atomic density is varied gradually by changing the temperature of the sodium oven while the input intensity is modulated slowly at about 50 Hz. This rate is many orders of magnitude slower than the dynamic rates of the system (κ, $\gamma_\parallel$ $\gamma_\perp$, and v), thereby ensuring the observation of steady states. The input and output powers (P_i versus P_t) are continuously monitored. We record the resonant conditions, and infer $\alpha_m L$ by observing the monitor absorption (P_m) and the peak optical-pumping fluorescence ($I_{\rm OP}$). A direct measurement of the cooperativity parameter C can be made by taking the ratio of the input switching points in resonant absorptive bistability,[14] so we record the hysteresis cycle to obtain the ratio and compare it to the calculated values of C based on the measurement of the signal absorption $\alpha_m L$ and the finesse F.

For comparisons with the theory we define, following Drummond,[19] the normalized input (y^2) and output ($|x|^2$) intensities and the cooperativity C as follows:

$$y^2 = f_1 \frac{T_0 P_i}{\pi w_0^2 I_s T}, \quad |x|^2 = f_1 \frac{P_t}{\pi w_0^2 I_s T}, \quad C = f_2 \frac{\alpha_m L F}{2\pi}, \tag{5.1}$$

where $f_1 = 2$ and $f_2 = \frac{1}{2}$ for the ring cavity, while $f_1 = 6$ and $f_2 = 1$ for the standing-wave cavity. I_s is the saturation intensity of the atomic transition, F is the finesse of the resonator, and T_0 is the empty cavity transmission. The cavity detuning Θ and the atomic detuning Δ are given, as already defined, by

$$\Theta = \frac{\omega_C - \omega_{\rm in}}{\kappa}, \quad \Delta = \frac{\omega_A - \omega_{\rm in}}{\gamma_\perp}, \tag{5.2}$$

where $\omega_{\rm in}$ is the frequency of the incident field, ω_C the frequency of the cavity mode, and ω_A the atomic transitions frequency; κ is the cavity decay rate and $\gamma_\perp$ the polarization decay rate.

The parameter C can be calculated from (i) measured quantities using the calibrations of the optical pumping, monitor absorption, and cavity losses, and (ii) the ratio of the input switching points in resonant absorptive bistability. Previous experiments[14,15] have shown that these two methods are consistent with one another. For experiments (d) and (e) our measurements of C are based solely on the ratios. The second method is particularly useful in the ring configuration where the atomic medium is crossed four times and a transverse standing wave pattern is formed where the light beams intersect. The calibrations, performed with only one pass through the medium, do not permit a direct calculation of C.

When the ratio of input turning points in the resonant

absorptive case in around two, both the atomic and cavity detunings are changed from zero with $\Delta\Theta < 0$. As the instability develops, the input-output characteristics (Fig. 13) change dramatically since the mean value of the pulsating state is displaced above the corresponding time-independent steady state. Note the similarity between Fig. 13(a) and the theoretical predictions [Figs. 5(b) and 5(c)]. The spectrum of the photocurrent from PMT(f) shows a coherent spike which shifts frequency as the cavity is detuned or as the input intensity is scanned. The cavity length (cavity detuning) and the frequency of the signal laser may be fixed, and the input intensity varied to locate the instability boundary as a function of the input-output parameters [Fig. 13(a)], with its corresponding associated frequency as seen in Fig. 13(b).

By changing the cavity and laser detunings at a given value of C, we explore the instability boundary in the (Θ,Δ) plane. Later, we can make absolute comparisons with the theory, with no adjustable parameters. The process is repeated for different atomic densities C by slowly changing the temperature of the oven.

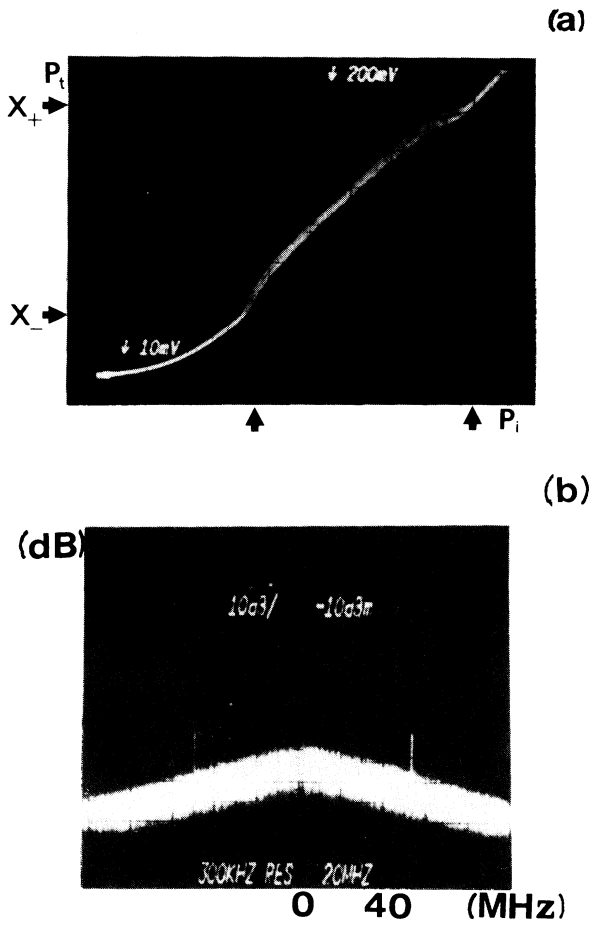

FIG. 13. (a) Input-output characteristics (P_i vs P_t) as recorded on an oscilloscope; the fuzzy region limited by the arrows indicated the presence of an instability; (X_+,X_-) limit the instability in the transmitted intensity. No bistability is present. (b) Spectrum-analyzer trace of the photocurrent from PMT(f) in the presence of an instability for fixed input intensity. The spikes around 50 MHz indicate an instability. Both traces are taken with the standing-wave cavity *e*. The parameters are $C=50\pm10$, $\Theta=-25\pm1$, $\Delta=2.5\pm0.5$, $\kappa'=0.32$, and $\gamma=1.6$.

C. Verification of the instability of a single spatial mode

Before proceeding with a discussion of the results and a comparison with the theory it is necessary to stress the single-mode characteristic of our system under self-pulsing conditions. To test experimentally the presence of only the fundamental TEM_{00} mode, we scan the transverse profile of the far-field output beam with an aperture and examine the oscillatory structure as a function of the radial coordinate. Preliminary measurements ($\pm25\%$) in the ring (d) configuration indicate a TEM_{00} mode for the pulsating part of the output from the cavity.[33] Measurements in the standing wave configuration (e) are presented here.

The cavity is locked to a red transmittion peak about 40 MHz away from the yellow resonance using standard lock-in techniques and a double-pass AOM. The signal laser is detuned to a given frequency which is monitored by recording the optical-pumping fluorescence and the independent cavity scan. A clear unstable region is identified, as in Fig. 13, and the input intensity fixed midway inside the unstable region. The output beam is split onto two fast photomultiplier tubes (Fig. 14). The whole beam is focused onto PMT(1) and its photocurrent is ac coupled and amplified to serve as the local oscillator (LO) port of a rf mixer. This signal is also monitored in a spectrum analyzer to insure that neither the amplitude nor the frequency of oscillation change during the measurement.

The other beam ($2w=4$ mm) is directed towards a circular aperture with diameter 0.6 mm which can be translated horizontally and vertically. The light that passes is detected by PMT(2). This signal is amplified, ac coupled, and used as the ratio frequency signal port (S) of the mixer. The amplified signal is also directed towards an oscilloscope without ac coupling to give a reading of the average power transmitted by the cavity as a function of the transverse coordinate (that is, for varying position

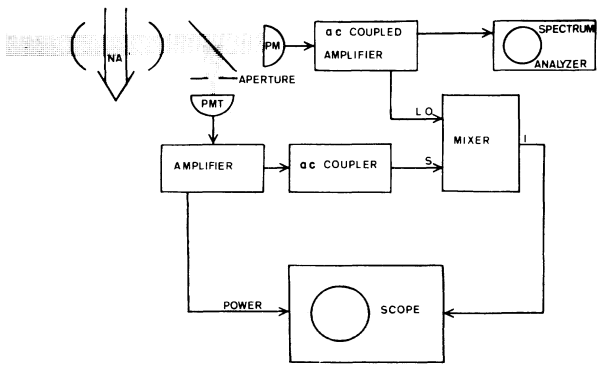

FIG. 14. Experimental arrangement for measurement of the transverse profile of the oscillatory part of the output beam.

of the aperture). This measurement works as well in the absence of self-pulsing. The phase difference between the LO and S ports of the mixer is varied by introducing delays in the cables taking the signals from the amplifiers to the mixer, and is optimized to produce a mixing signal at the output port (I) with the aperture centrally located. The intermediate frequency port (I) is the output of the mixer and is displayed on an oscilloscope. I is proportional to the product of the rms amplitude of the current from the apertured beam and the cosine of the phase difference between the oscillatory current and the local oscillator current. The output I gives both the spatial profile of the pulsing state as well as any phase dependence of the oscillations across the beam, as might occur for an alternation between TEM_{00} and TEM_{pq} modes.

Figure 15 presents the average power and the output I as functions of the position of the aperture. This figure shows that the output mode is mainly a TEM_{00} mode, that the whole beam is oscillating at the frequency measured with PMT(1), and that the phase of the output beam is uniform across the transverse profile. Figure 15 corresponds to a horizontal scan across the center in an oscillatory state which corresponds closely to the one depicted in Fig. 15, for a fixed input intensity around the center of the oscillating region and $C=50\pm10$, $\Delta=2.0\pm0.5$, and $\Theta=-21\pm1$. The results are similar as the vertical position of the aperture is varied. We conclude that even in the self-pulsing state we have only a single transverse and a single longitudinal mode interacting with the atoms inside the cavity.

D. Comparison with theory

We start with an exploration of the instability boundaries in the detuning space (Θ,Δ). Figures 16–18

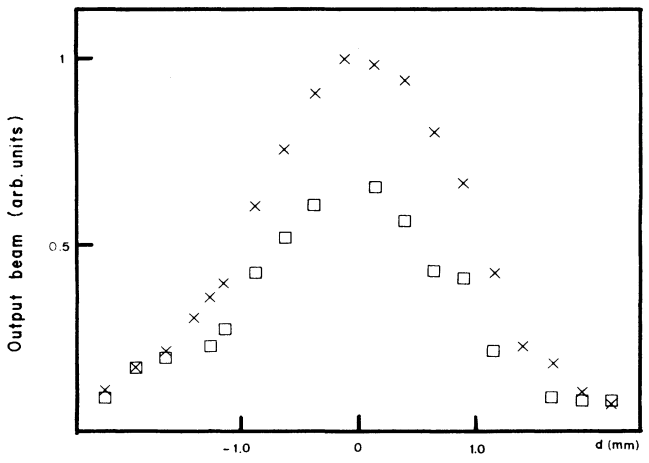

FIG. 15. Transverse profile of the output beam. The ×'s represent the average power as a function of aperture position when the system is self-pulsing ($C=50\pm10$, $\Theta=-21\pm1$, $\Delta=-2\pm0.5$, $\kappa'=0.32$, and $\gamma=1.6$). The squares are the output of the rf mixer as a function of aperture position; this signal is proportional to just the oscillatory part of the output beam and to any phase difference between the spatially resolved oscillations and the whole beam oscillations. Measurements done with cavity e.

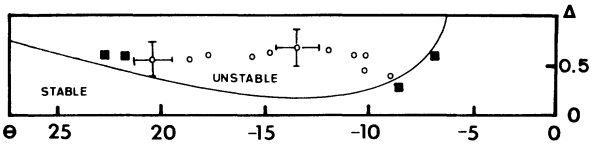

FIG. 16. Domain of instability in the detuning space for $C=95\pm5$; open circles indicate instability; closed squares imply stability; above the continuous line is the theoretically unstable region. The confocal standing-wave resonator a is used with $\kappa'=0.4$ and $\gamma=1.6$. The systematic uncertainties in the detunings are $\pm10\%$.

present our measurements for three different cavities with given values of C. These measurements are done holding the atomic detuning constant and varying the cavity detuning. The boundaries of the instability are found following the procedure described in Refs. 22 and 34.

We have assumed[14,15,35] that transit broadening is a homogeneous process which modifies the polarization decay rate $\gamma_\perp/2\pi$ from 5 to 6.25 MHz (thus $\gamma=1.6$), changing the saturation intensity (I_s) from 6.4 to 7.3 mW/cm^2. This is an approximation which is not fully justified, but we have found that in resonant absorptive bistability, the difference between the full theoretical calculation of the transit-broadened system (obtained by integrating the Maxwell-Bloch equations as the atoms traverse the Gaussian mode of the cavity) and the homogeneous approximation used here[14] for the input switching points is less than 10% along the lower branch and 3% along the upper branch. For small cavity detunings and atomic detunings the approximation gives good quantitative agreement with experiments.[15] The inhomogeneous broadening present (less than 1 MHz) due to imperfect collimation of the atomic beams is neglected.

The theory of Ref. 22 is for a ring cavity and the experimental results of Fig. 16 are in a standing-wave one. Therefore we draw no further conclusions from the comparison. Figures 17 and 18 are for ring configurations and they do represent absolute quantitative comparisons

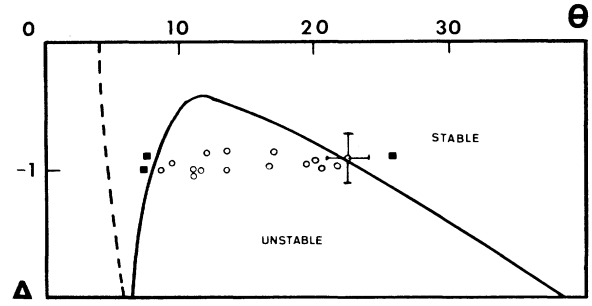

FIG. 17. Domain of instability in the detuning space for $C=60\pm5$, $\kappa'=0.5$, and $\gamma=1.6$. Open circles indicate instability, closed squares stability. Below the continuous line is the unstable region based on the Gaussian theory, while to the right of the dashed line is the plane-wave prediction of the unstable region. The ring cavity c is used in this measurement. Systematic uncertainties in the detunings are $\pm10\%$.

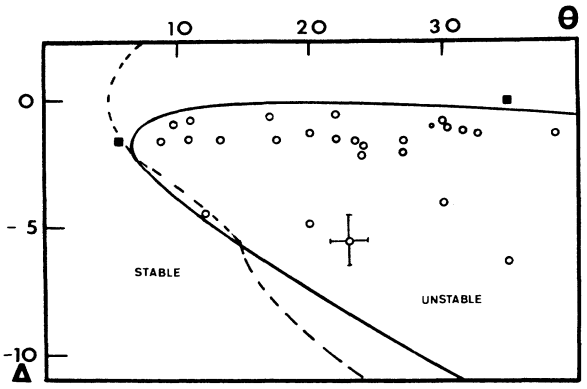

FIG. 18. Domain of instability in the detuning space for $C=300\pm50$, $\kappa'=0.4$, and $\gamma=1.6$. Open circles indicate instability, closed squares stability. Inside the continuous line is the unstable region predicted by the Gaussian theory, while to the right of the dashed line is the plane-wave prediction of the unstable region. The ring *d* cavity is used in this measurement. Systematic uncertainties in the detunings are $\pm10\%$.

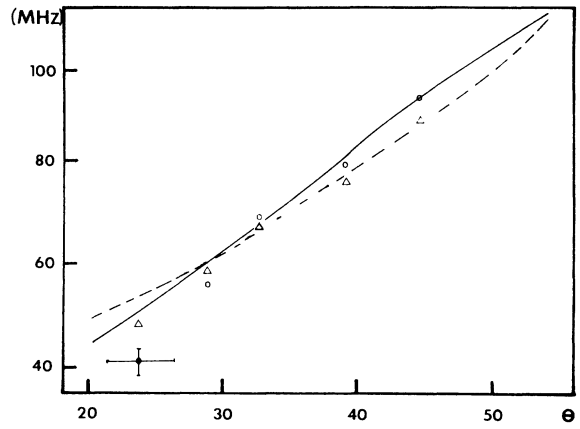

FIG. 19. Frequencies of oscillation (ν_+,ν_-) associated with the output-intensity boundaries of instability (X_+,X_-) in Fig. 13(a), for $C=106\pm5$, $\Delta=-2.2\pm0.2$, $\kappa'=0.32$, and $\gamma=1.6$ as a function of cavity detuning Θ in the out-of-confocal geometry *b*. Triangles are taken at the low-intensity boundary (X_-), circles are taken at the high-intensity boundary (X_+). From the model of Lugiato *et al.* (Ref. 22) the dashed line shows the frequency (ν_-) at the low-intensity boundary (X_-) while the continuous line is the frequency (ν_+) at the high-intensity boundary (X_+). Systematic uncertainties in the detunings are $\pm10\%$.

(without adjustable parameters) with the appropriate theory of Ref. 22. In Figs. 17 and 18 we also present the predictions from the plane-wave theory. The instability domain is wider and in clear disagreement with our experimental results. Although our measurements are represented in Figs. 16–18 by isolated points in the (Θ,Δ) plane, we move experimentally from one point to the other continuously, so we have in fact explored the boundaries in much greater detail than a single point may indicate in the figures.

The value of C in Fig. 18 is more than 30 times that of the critical onset of absorptive bistability. The validity of the uniform field limit may be questionable, since $\alpha_m L$ is now about 12 for the four-pass ring configuration [Fig. 12(a)]. The work of Snapp[36] on instabilities without the uniform field limit and in the plane-wave model shows that the small parameter for the uniform field approximation is $\alpha L/(1+\Delta^2+|x|^2)$. For the parameters of Fig. 18, $|x|^2$ is around 200, so we believe the limit is still fulfilled. However, the problem may be present at lower intensities.

As one can see from Fig. 13(a) there are two instability limits in the output intensity, marked X_+,X_- for a given point in the (Θ,Δ) plane, except when one is at a boundary such as those marked by the solid lines in Figs. 16-18, where the two limit intensities collapse into a single one. With each intensity (X_+,X_-) there is an associated frequency of oscillation (ν_+,ν_-). We map these frequencies as the cavity detuning is changed, with fixed values of the atomic detuning Δ and of the cooperativity parameter C. The results with the (b) cavity configuration are presented in Fig. 19. In spite of the standing-wave geometry of the experiment, the agreement with the ring-cavity theory is reasonable, especially in illustrating the inversion of frequencies as a function of increasing cavity detuning. The output intensities at the lower limit point (X_-) and at the upper point (X_+) can differ by as much as a factor of 5, while the frequencies change by only 20% at most; the correlation between the oscillation frequency and the cavity detuning parameter Θ seems to support the simple explanation of the instability as arising from gain at the cavity resonance frequency,[37] which gives a good estimate of the frequency of oscillation at least for the range of decay ratio (κ') that we have explored experimentally. In the observations of the frequency spectrum, higher harmonics are present for values of the cooperativity parameter C larger than 100, and certain values of the detuning parameters and input intensity, but we have not carried out a careful quantification of such regions. When the output of PMT(f) is displayed on an oscilloscope, the depth of modulation of the self-pulsing state can be as large as 7 to 1 and, with all the parameters fixed, persists for long periods of time (minutes) (Fig. 20).

E. Other observations

Over the range of parameters explored in these experiments ($0<|\Delta|<6$, $0<|\Theta|<40$, $C<350$), and with resonators having decay rates slower than the polarization decay rate by roughly a factor of 2, no higher-order bifurcations of the self-pulsing states[21] were identified in the high intracavity intensity regions (upper branch). Under certain circumstances the cavity field began circulating in both directions with the ring cavities (c) and (d) for unidirectional excitation, as if the gain present was able to produce laser action in the counterpropagating sense of rotation even without population inversion;[37(c)] the mode structure of the counterpropagating beam changed from a TEM_{00} mode to a higher transverse structure under

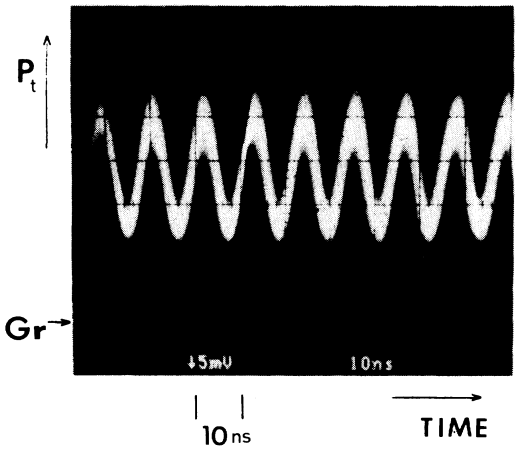

FIG. 20. Oscilloscope trace of the output intensity as a function of time when the system is self-pulsing for fixed values of C, input intensity, and atomic and cavity detunings. The pulsations are quite stable over periods of minutes.

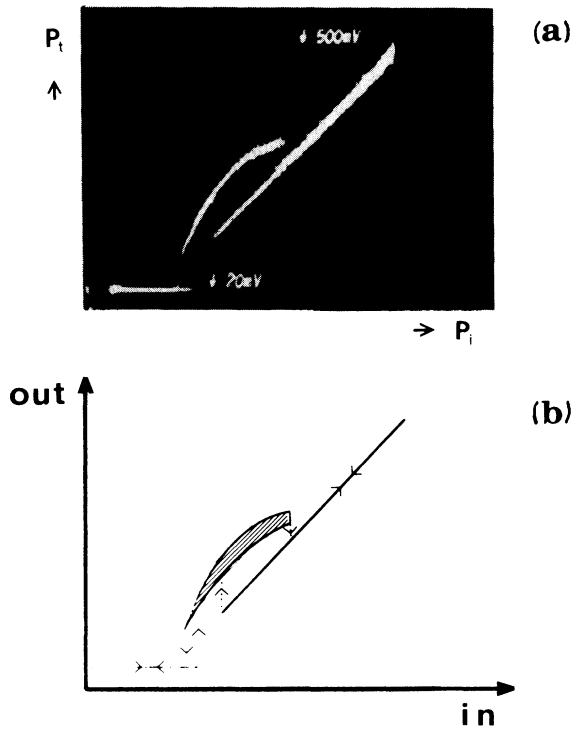

FIG. 21. (a) Input-output characteristics (P_i vs P_t) for $C=250\pm50$, $\Theta=14\pm3$, $\Delta=-3.0\pm1.0$, $\kappa'=0.4$, and $\gamma=1.6$ in the ring d cavity, when a hard-mode instability is present, giving rise to a new bistable region associated with the oscillatory state. (b) Explanatory drawing of the instability as an arch separated from the upper branch, the arrows indicating the direction of switching as the input intensity is scanned at a rate of 50 Hz.

conditions which we cannot quantify precisely. Sometimes one could correlate one of the multiple branches of the input-output characteristics with the appearance of the counterpropagating beam.

Figure 21(a) is a photograph of the input-output characteristics for the ring cavity (d) when hysteresis is present in the unstable region; we interpret this effect as the result of a hard-mode excitation in the sense that the system becomes unstable only in the presence of a finite size perturbation. Figure 21(b) provides our explanation of the photograph for the instability that gives rise to a new hysteresis cycle associated with oscillatory states. This corresponds to the behavior predicted in Fig. 6.

With the ring cavity (d), for high values of the cooperativity parameter ($C>250$) and atomic detuning ($|\Delta|>5$), sometimes two simultaneous spikes are present in the frequency analyzer with a separation of less than 10 MHz; in this case their low-frequency beat note is also present.

Although we have seen mode reshaping along the upper branch by monitoring the transverse profile of the output field with a reticon (D in Fig. 10) for cavity and atomic detuning of the same sign, we have observed no indication of dynamic instability associated with the reshaping. For opposite signs of atomic and cavity detuning, when the instability is favored, mode reshaping is not present in the high intracavity intensity region, and the instabilities persist independent of which detuning is negative. We thus believe that self-focusing and mode reshaping do not play a fundamental role in this experimental observation of the single-mode instability of optical bistability.

VI. CONCLUSIONS

In the theoretical sections of this paper we established the physical conditions under which the single-mode description of optical bistability holds. We proposed two different formulations of the single-mode model; one assumes the plane-wave approximation, the other that the output field retains the same Gaussian radial profile of the input field.

The experiments confirm the results of the Gaussian formulation: not only does the output field maintain a Gaussian shape even in the regime of the spontaneous oscillations, but the boundaries of the instability domain in parameter space and the oscillation frequency are both in good agreement with the predictions of the Gaussian model. The plane-wave formulation, instead, turns out to be inadequate.

In agreement with the experiments, the Gaussian model displays no period 2,4, . . . , etc. and chaotic structures which are a characteristic prediction of the plane-wave model. The only higher-order temporal structure of the Gaussian formulation is an envelope breathing that corresponds to a two-frequency operation. We remark in this connection that the same phenomenon, i.e., the disappearance of period-n ($n>1$ and chaotic patterns, is common also to the laser with an injected signal if the input beam has a Gaussian shape and under the conditions and physical parameter range analyzed in Ref. 28 for the plane-wave limit.

ACKNOWLEDGMENTS

This work has been partially supported by a NATO Research Grant and by the European Economic Community (EEC) twinning project on dynamics of nonlinear optical systems. The work of three of us (L.A.O., H.J.K. and A.T.R.) was supported by the National Science Foundation, the Venture Research Unit of British Petroleum, and by the Joint Services Electronic Program.

---

*Present address: Department of Physics, Harvard University, Cambridge, MA 02138.

[1]Feature issue on *Instabilities in Active Optical Media,* J. Opt. Soc. Am. B **2** (1985).

[2]*Optical Instabilities,* edited by R. W. Boyd, M. G. Raymer, and L. M. Narducci (Cambridge University Press, New York, 1986).

[3]L. A. Lugiato, in *Progress in Optics,* edited by E. Wolf (North-Holland, Amsterdam, 1984), Vol. XXI, p. 69.

[4]J. C. Englund, R. R. Snapp, and W. C. Schieve, in *Progress in Optics,* edited by E. Wolf, (North-Holland, Amsterdam, 1984), Vol. XXI, p. 335.

[5]H. J. Carmichael, in *Laser Physics,* Vol 182 of *Lecture Notes in Physics,* edited by J. D. Harvey and D. F. Walls (Springer-Verlag, Berlin, 1983), p. 64.

[6]P. Mandel, in *Frontiers in Quantum Optics,* edited by R. Pike and S. Sarkar, (Hilger, Bristol, 1986).

[7]N. B. Abraham, P. Mandel, and L. M. Narducci, in *Progress in Optics,* edited by E. Wolf (North-Holland, Amsterdam, 1988), Vol. XXV.

[8]See, for example, L. W. Casperson, J. Opt. Soc. Am. B **2**, 62 (1985); **2**, 73 (1985); L. M. Hoffer, T. H. Chyba, and N. B. Abraham, *ibid.* **2**, 102 (1985); N. B. Abraham, in *Optical Instabilities,* edited by R. W. Boyd, M. G. Raymer, and L. M. Narducci (Cambridge University Press, New York, 1986), p. 46.

[9]A. V. Uspenskii, Radio Eng. Electron. Phys. (USSR) **8**, 1145 (1963); **9**, 605 (1964); V. V. Korobkin and A. V. Uspenskii, Zh. Eksp. Teor. Fiz. **45**, 1003 (1963) [Sov. Phys.—JETP **18**, 693 (1964)]; A. Z. Grazyuk and A. N. Oraevsky, in *Quantum Electronics and Coherent Light,* edited by P. A. Miles (Academic, New York, 1964), p. 192; A. Z. Grazyuk and A. N. Oraevsky, Radio Eng. Electron. Phys. (USSR) **9**, 424 (1964).

[10]H. Haken, Z. Phys. **190**, 327 (1966); H. Risken, C. Schmid, and Weidlich, Z. Phys. **194**, 337 (1966).

[11]H. Haken, Phys. Lett. **53A**, 77 (1975).

[12]E. N. Lorenz, J. Atmos. Sci. **20**, 130 (1963).

[13](a) L. A. Lugiato, F. Prati, D. K. Bandy, L. M. Narducci, P. Ru, and J. R. Tredicce, Opt. Commun. **64**, 167 (1987); (b) L. A. Lugiato, F. Prati, L. M. Narducci, P. Ru, J. R. Tredicce, and D. K. Bandy, Phys. Rev. A **37**, 3847 (1988).

[14](a) A. T. Rosenberger, L. A. Orozco, and H. J. Kimble, Phys. Rev. A **28**, 2596 (1983); (b) L. A. Orozco, H. J. Kimble, and A. T. Rosenberger, Opt. Commun. **62**, 53 (1987).

[15]L. A. Orozco, A. T. Rosenberger, and H. J. Kimble, Phys. Rev. A **36**, 3248 (1987).

[16](a) R. Bonifacio and L. A. Lugiato, Opt. Commun. **19**, 172 (1976); (b) R. Bonifacio and L. A. Lugiato, Lett. Nuovo Cimento **21**, 517 (1978).

[17]R. J. Ballagh, J. Cooper, M. W. Hamilton, W. J. Sandle, and D. M. Warrington, Opt. Commun. **37**, 143 (1981).

[18]E. Arimondo, A. Gozzini, F. Lovitch, and E. Pistelli, in *Optical Bistability,* edited by C. M. Bowden, M. Ciftan, and H. R. Robl (Plenum, New York, 1981).

[19]P. D. Drummond, IEEE J. Quantum Electron. **QE-17**, 301 (1981).

[20]L. A. Lugiato and M. Milani, Z. Phys. B **50**, 171 (1983); in *Optical Bistability II,* edited by C. M. Bowden, H. M. Gibbs, and S. L. McCall (Plenum, New York, 1984), p. 397.

[21]L. A. Lugiato, L. M. Narducci, D. K. Bandy, and C. A. Pennise, Opt. Commun. **43**, 281 (1982); L. A. Lugiato and L. M. Narducci, in *Coherence and Quantum Optics V,* edited by L. Mandel and E. Wolf (Plenum, New York, 1984), p. 941.

[22]L. A. Lugiato, R. J. Horowicz, G. Strini, and L. M. Narducci, Phys. Rev. A **30**, 1366 (1984).

[23]L. A. Orozco, A. T. Rosenberger, and H. J. Kimble, Phys. Rev. Lett. **53**, 2547 (1984).

[24]L. M. Narducci, J. R. Tredicce, L. A. Lugiato, N. B. Abraham, and D. K. Bandy, Phys. Rev. A **32**, 1588 (1985).

[25]L. A. Lugiato, Opt. Commun. **32**, 108 (1980); L. A. Lugiato, Z. Phys. B **41**, 85 (1981); L. M. Narducci, J. R. Tredicce, L. A. Lugiato, N. B. Abraham, and D. K. Bandy, Phys. Rev. A **32**, 1588 (1985).

[26]R. Bonifacio and L. A. Lugiato, Lett. Nuovo Cimento **21**, 505 (1978); **21**, 510 (1978).

[27]S. L. McCall, Appl. Phys. Lett. **32**, 284 (1978).

[28]K. Ikeda, Opt. Commun. **30**, 257 (1979); K. Ikeda and O. Akimoto, Phys. Rev. Lett. **48**, 617 (1982).

[29]See, for example, H. Haken, *Synergetics—An Introduction,* 3rd ed. (Springer-Verlag, Berlin, 1983), p. 123.

[30]See, for example, H. Kogelnik and T. Li, Appl. Opt. **5**, 1550 (1966); H. Kogelnik, in *Lasers: A Series of Advances,* edited by A. K. Levine (Marcel Dekker, New York, 1966), Vol. I, p. 265.

[31]P. Ru, L. M. Narducci, J. R. Tredicce, D. K. Bandy, and L. A. Lugiato, Opt. Commun. **63**, 310 (1987).

[32]J. A. Abate, Opt. Commun. **10**, 269 (1974); M. L. Citron, H. R. Gray, C. W. Gabel, and C. R. Stroud, Jr., Phys. Rev. A **16**, 1507 (1977).

[33]L. A. Orozco, M. G. Raizen, A. T. Rosenberger, and H. J. Kimble, in *Optical Bistability III,* edited by H. M. Gibbs, P. Mandel, N. Peyghambarian, and S. D. Smith (Springer-Verlag, Berlin, 1986), p. 307.

[34]L. A. Orozco, K. A. Jones, A. T. Rosenberger, and H. J. Kimble (unpublished).

[35]A. T. Rosenberger, L. A. Orozco, H. J. Kimble, and P. D. Drummond (unpublished).

[36]R. R. Snapp, Ph.D. dissertation, University of Texas at Austin, 1986.

[37](a) B. R. Mollow, Phys. Rev. A **5**, 2217 (1972); (b) F. Y. Wu, S. Ezekiel, M. Ducloy, and B. R. Mollow, Phys. Rev. Lett. **38**, 1077 (1977); (c) A. M. Bonch-Bruevich, V. A. Khodovoi, and N. A. Chigir, Zh. Eksp. Theor. Fiz. **67**, 2069 (1974) [Sov. Phys.—JETP **40**, 1027 (1975)].

[38]D. K. Bandy, L. M. Narducci, and L. A. Lugiato, J. Opt. Soc. Am. B **2**, 148 (1985).

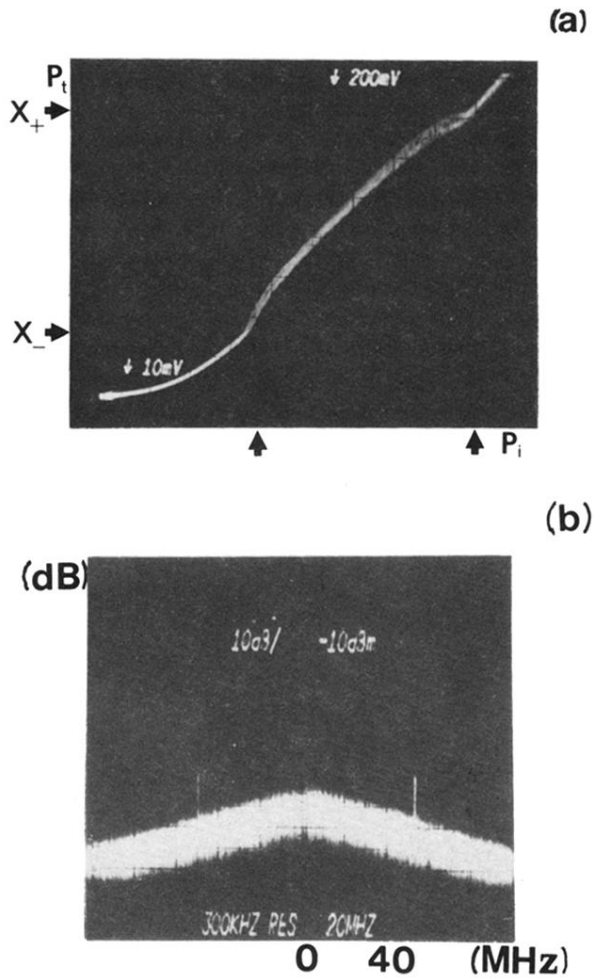

FIG. 13. (a) Input-output characteristics (P_i vs P_t) as recorded on an oscilloscope; the fuzzy region limited by the arrows indicated the presence of an instability; (X_+,X_-) limit the instability in the transmitted intensity. No bistability is present. (b) Spectrum-analyzer trace of the photocurrent from PMT(f) in the presence of an instability for fixed input intensity. The spikes around 50 MHz indicate an instability. Both traces are taken with the standing-wave cavity *e*. The parameters are $C=50\pm10$, $\Theta=-25\pm1$, $\Delta=2.5\pm0.5$, $\kappa'=0.32$, and $\gamma=1.6$.

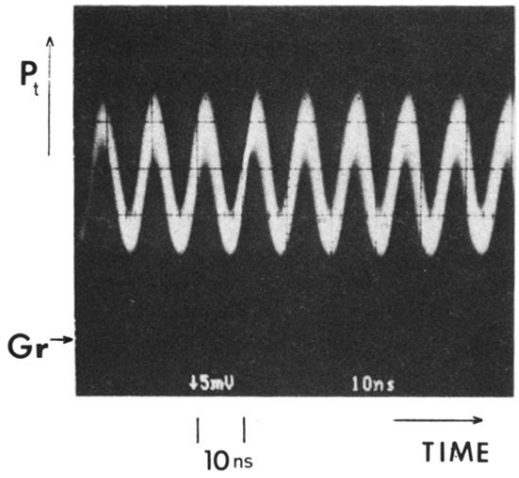

FIG. 20. Oscilloscope trace of the output intensity as a function of time when the system is self-pulsing for fixed values of C, input intensity, and atomic and cavity detunings. The pulsations are quite stable over periods of minutes.

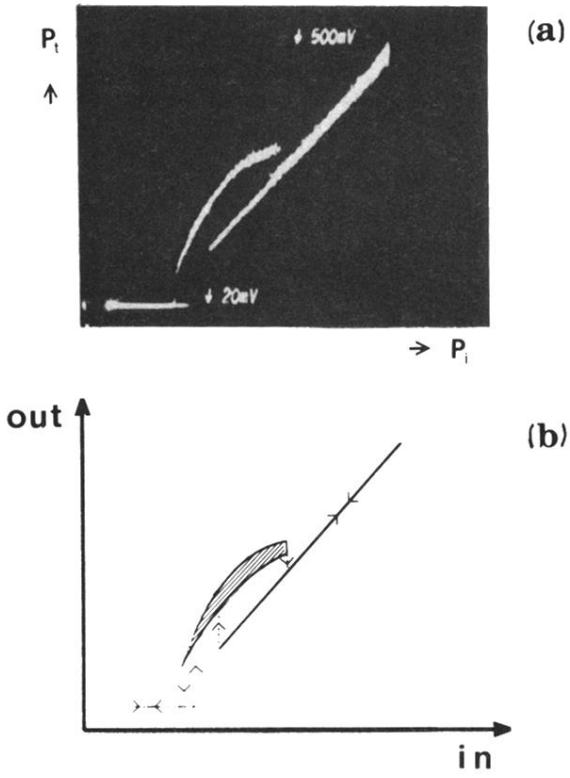

FIG. 21. (a) Input-output characteristics (P_i vs P_t) for $C=250\pm50$, $\Theta=14\pm3$, $\Delta=-3.0\pm1.0$, $\kappa'=0.4$, and $\gamma=1.6$ in the ring d cavity, when a hard-mode instability is present, giving rise to a new bistable region associated with the oscillatory state. (b) Explanatory drawing of the instability as an arch separated from the upper branch, the arrows indicating the direction of switching as the input intensity is scanned at a rate of 50 Hz.